International Journal of Biological Macromolecules 266 (2024) 131359

Contents lists available at ScienceDirect

International Journal of Biological Macromolecules

journal homepage: www.elsevier.com/locate/ijbiomac

PEGylated chitosan-coated nanophotosensitizers for effective cancer treatment by photothermal-photodynamic therapy combined with glutathione depletion

Yu-Hsin Chen [a], I-Ju Liu [a], Tzu-Chen Lin [a], Min-Chen Tsai [a], Shang-Hsiu Hu [b], Tsai-Ching Hsu [c,d,e], Yi-Ting Wu [c], Bor-Show Tzang [c,d,e,f,*], Wen-Hsuan Chiang [a,**]

[a] Department of Chemical Engineering, National Chung Hsing University, Taichung 402, Taiwan
[b] Department of Biomedical Engineering and Environmental Sciences, National Tsing Hua University, Hsinchu 300, Taiwan
[c] Institute of Medicine, Chung Shan Medical University, Taichung 402, Taiwan
[d] Immunology Research Center, Chung Shan Medical University, Taichung 402, Taiwan
[e] Clinical Laboratory, Chung Shan Medical University Hospital, Taichung 402, Taiwan
[f] Department of Biochemistry, School of Medicine, Chung Shan Medical University, Taichung 402, Taiwan

ARTICLE INFO

Keywords:
PEGylated chitosan
Photothermal-photodynamic therapy
Nanophotosensitizer

ABSTRACT

The combination of photothermal therapy (PTT) and photodynamic therapy (PDT) has emerged as a promising strategy for cancer treatment. However, the poor photostability and photothermal conversion efficiency (PCE) of organic small-molecule photosensitizers, and the intracellular glutathione (GSH)-mediated singlet oxygen scavenging largely decline the antitumor efficacy of PTT and PDT. Herein, a versatile nanophotosensitizer (NPS) system is developed by ingenious incorporation of indocyanine green (ICG) into the PEGylated chitosan (PEG-CS)-coated polydopamine (PDA) nanoparticles via multiple π-π stacking, hydrophobic and electrostatic interactions. The PEG-CS-covered NPS showed prominent colloidal and photothermal stability as well as high PCE (ca 62.8 %). Meanwhile, the Michael addition between NPS and GSH can consume GSH, thus reducing the GSH-induced singlet oxygen scavenging. After being internalized by CT26 cells, the NPS under near-infrared laser irradiation produced massive singlet oxygen with the aid of thermo-enhanced intracellular GSH depletion to elicit mitochondrial damage and lipid peroxide formation, thus leading to ferroptosis and apoptosis. Importantly, the combined PTT and PDT delivered by NPS effectively inhibited CT26 tumor growth in vivo by light-activated intense hyperthermia and redox homeostasis disturbance. Overall, this work presents a new tactic of boosting antitumor potency of ICG-mediated phototherapy by PEG-CS-covered NPS.

1. Introduction

Near-infrared (NIR)-triggered phototherapy based on the use of NIR light in combination with photosensitizers (PS) has emerged as a promising strategy for cancer treatment due to its capability for selective damage of tumor sites with minimal adverse effects [1–10]. Photodynamic therapy (PDT) and photothermal therapy (PTT) are highly potential therapeutic methods in phototherapy and have displayed great potential as minimally invasive techniques for clinical cancer treatment [1–10]. In the PDT-mediated treatment process, the utilized small-molecule PS exposed to NIR laser irradiation can transform surrounding molecular oxygen (O_2) into toxic reactive oxygen species (ROS) such as singlet oxygen ($^1O_2$), thus eliciting the apoptosis of cancer cells [5,8,9]. Unfortunately, in addition to the tumor hypoxia (below 2 % O_2) highly resistant to PDT, glutathione (GSH), a key intracellular antioxidant, overexpressed with several-fold higher concentration (up to 10 mM) in cancer cells than that in normal cells, can largely scavenge ROS, thus lowering the anticancer potency of PDT [11,12]. Distinct from PDT, PTT utilizes heat generated from the NIR-induced energy conversion of a photothermal agent to directly ablate cancer cells [5,13,14]. However, PTT usually cannot completely inhibit tumor growth due to non-uniform heat transfer and distribution within the tumor, thus leading to tumor recurrence [15,16]. Recently, to conquer the limitations associated with a single phototherapy modality, considerable efforts to combine PDT

* Correspondence to: B.-S. Tzang, Institute of Medicine, Chung Shan Medical University, Taichung 402, Taiwan.
** Corresponding author.
E-mail addresses: bstzang@csmu.edu.tw (B.-S. Tzang), whchiang@dragon.nchu.edu.tw (W.-H. Chiang).

https://doi.org/10.1016/j.ijbiomac.2024.131359
Received 21 January 2024; Received in revised form 12 March 2024; Accepted 1 April 2024
Available online 4 April 2024

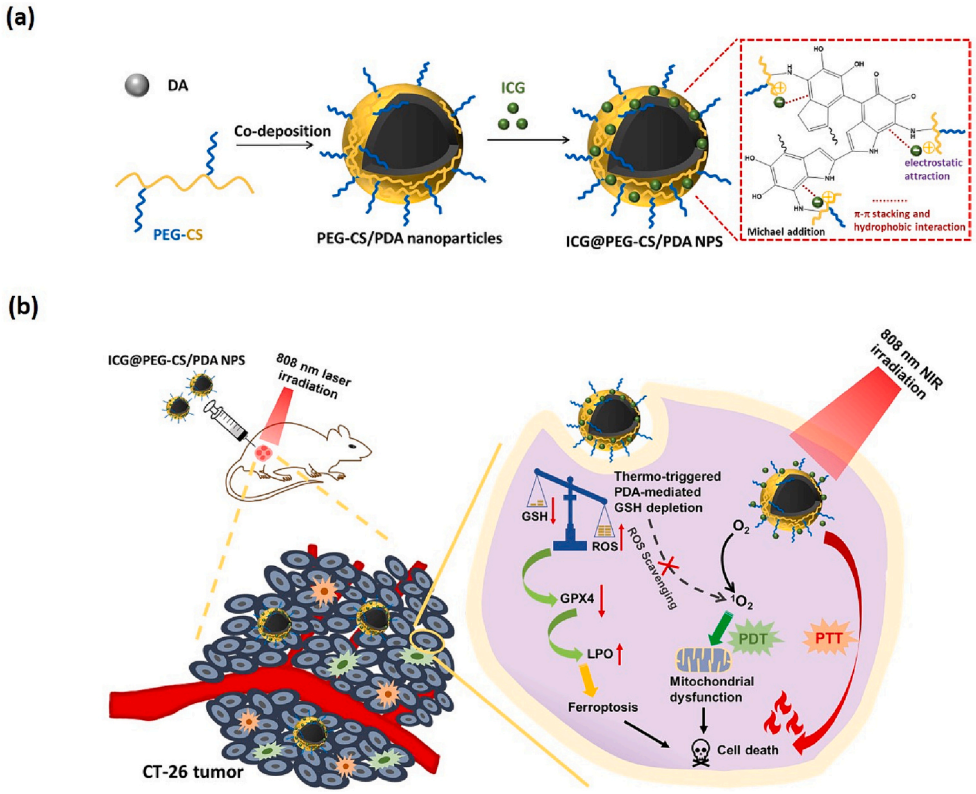

Scheme 1. Illustration of (a) fabrication of ICG@PEG-CS/PDA NPS and (b) their antitumor mechanisms via PTT/PDT-mediated manner combined with ferroptosis.

with PTT have accomplished significantly enhanced therapeutic efficacy [1–10]. Several studies demonstrate that the adequate local hyperthermia provided by PTT promotes intratumoral blood flow and oxygenation, being beneficial for PDT, while PDT-mediated ROS sensitize cancer cells to the hyperthermia produced by PTT [5,7,15].

In the past decade, to achieve effective tumor-targeted delivery of the combined PTT and PDT for augmented therapeutic outcomes, various nanoparticles including liposomes [17], silica nanoparticles [18], polymeric micelles and nanoparticles [19–21] have been developed as vehicles of small-molecule PS. For example, as reported by Zhang's group [22], the PpIX (PS for PDT) and IR-820 (PS for PTT) were encapsulated into liposomes to attain PpIX-IR-820@liposomes. Under irradiation of 793 and 450 nm lasers, the PpIX-IR820@liposomes showed a PDT/PTT synergistic anticancer effect on HeLa cells, human cervical cancer cells. Guo et al. developed mitochondria-targeted theranosomes capable of carrying both chlorin e6 (Ce6, PS for PDT) and IR780 (PS for PTT and NIR imaging agent) to realize enhanced PDT and PTT efficacy under sequential 808 and 660 nm laser irradiation [23]. Furthermore, to effectively boost the therapeutic outcomes of combined PDT and PTT, the tumor acidity-responsive lipid membrane-enclosed perfluorooctyl bromide (PFOB) oil droplet nanoparticle surface modified with *N*-acetyl histidine-modified D-α-tocopheryl polyethylene glycol 1000 succinate (PFOB@IMHNPs) were fabricated, capable of co-delivering oxygen, mTHPC (PS for PDT) and IR780 (PS for PTT) into tumors [16]. Notably, with NIR irradiation at 808 and 660 nm, the combination of PDT and PTT utilizing PFOB@IMHNPs prominently suppressed the growth of TRAMP-C1 tumors through effective tumor-targeted cargo delivery and relief of tumor hypoxia. However, in the above studies, the combination of PTT and PDT involved the co-delivery of two different PS and use of two different lasers, thereby being not favorable to clinical application. Therefore, the design of a facile PS-carrying nanoplatform coupled with usage of single laser is important for the PTT/PDT-mediated clinical cancer treatment.

Indocyanine green (ICG) composed of two hydrophobic polycyclic parts and sulfonate groups is an amphiphilic and non-toxic compound [24]. As the NIR fluorescent dye, ICG has been approved by the United States (US) Food and Drug Administration (FDA) to detect liver malignancy or vascularization in clinical operation [24,25]. Additionally, so far ICG utilized as a small-molecule PS has been demonstrated to generate singlet oxygen and hyperthermia under single NIR irradiation, thus disrupting solid tumor via the combination of PDT and PTT [25,26]. However, ICG applications in cancer treatment has been limited due to lack of specific tumor targeting, fast body clearance (2–4 min) in vivo, self-aggregation under physiological conditions and poor photothermal stability [24,25].

To achieve the single laser-triggered ICG-mediated PTT and PDT, various polymeric nanoparticles-based ICG delivery systems have been created [27–30]. Among them, the bioinspired poly(dopamine) (PDA) nanoparticles have attracted considerable attention owing to the prominent biocompatibility, satisfied PCE and effective integration with diverse therapeutic agents [31–38]. Furthermore, it has been demonstrated that PDA nanoparticles can consume intracellular GSH upon Michael addition or Schiff reaction [39–41]. Despite some strategies of using hydrophilic poly(ethylene glycol) (PEG) or linear hyaluronate (HA) to decorate the surfaces of ICG-carrying PDA nanoparticles for improved colloidal stability and ICG-mediated cancer phototherapy [20,21,42–44], all these nanoparticles only displayed limited PCE (25–48 %) because the additional surface coating was not able to further enhance their PCE. Furthermore, the studies mentioned above [20,21,42–44] did not explore the impact of intracellular PDA-mediated GSH depletion on the accumulation of singlet oxygen and the formation of lipid peroxides (LPO). Actually, the effectiveness of ICG-based phototherapy was limited because of its low PCE and photothermal stability, as well as the scavenging of singlet oxygen by intracellular GSH. To address these issues, herein, the graft-type PEGylated chitosan (PEG-CS) conjugates were synthesized upon Schiff base reaction between chitosan

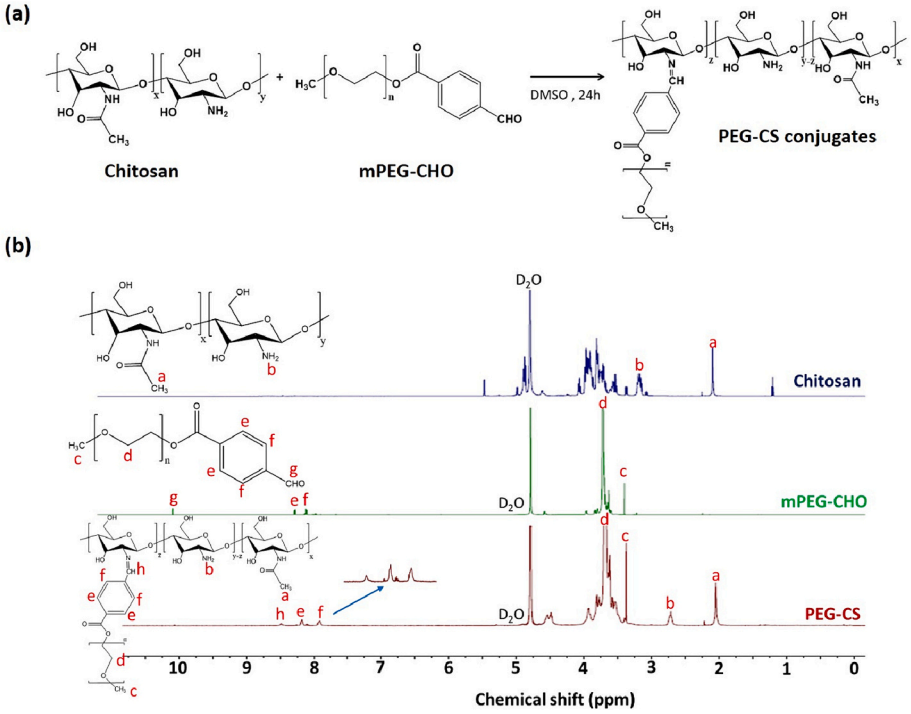

Fig. 1. (a) Synthetic pathway and chemical structure of PEG-CS conjugates. (b) ^{1}H NMR spectra of chitosan, mPEG-CHO and PEG-CS in D_2O.

and methoxy PEG benzaldehyde (mPEG-CHO), and utilized as a key coating material of nanophotosensitizers (NPS). Chitosan, a cationic polysaccharide produced from deacetylation of natural chitin, has been extensively utilized in the surface modification of various nanoparticles owing to its biocompatibility, biodegradability and pH-responsive properties [45,46]. Through simple co-deposition of dopamine molecules and PEG-CS conjugates in basic aqueous solution, the PEG-CS/PDA nanoparticles were attained as ICG vehicles (Scheme 1a). Next, a versatile NPS system was fabricated by ingenious incorporation of ICG into PEG-CS/PDA nanoparticles via multiple π-π stacking, hydrophobic and electrostatic interaction. Note that the PEG-CS conjugates coated on the surfaces of NPS remarkably promoted their PCE (ca 62.8 %), colloidal and photothermal stability. Also, the PEG-CS-coated NPS exhibited outstanding singlet oxygen-generating and PDA-mediated GSH-consuming capability, and sustained ICG release. After being internalized by CT26 cells, mouse colon adenocarcinoma cell line, these NPS under single 808 nm NIR laser irradiation produced massive singlet oxygen with the aid of hyperthermia-enhanced intracellular GSH consumption via PDA-mediated Michael reaction, thus promoting mitochondrial damage and LPO formation to provoke apoptosis and ferroptosis (Scheme 1b). The in vivo antitumor efficacy studies showed that these PEG-CS-decorated NPS potently inhibited CT26 tumor growth upon NIR-elicited hyperthermia and singlet oxygen generation without severe systemic toxicity. To the best of our knowledge, rare studies on the surface modification of ICG-carrying PDA nanoparticles with PEG-CS conjugates and their cancer treatment via PTT/PDT-mediated manner combined with ferroptosis were reported. Therefore, based on our findings, the PEG-CS-covered NPS show promising potential in the clinical cancer treatment of ICG-mediated phototherapy.

2. Experimental section

2.1. Materials

Dopamine·hydrochloride (DA) was acquired from Alfa Aesar (USA). Tris(hydroxymethyl) aminomethane (99 % for biochemistry) were supplied by Acros Organics (USA). ICG was purchased from Chem-Impex International (USA). Chitosan oligosaccharide (MW 5.0 kDa, 81 % degree of deacetylation) was obtained from Glentham Life Science Ltd. (UK). Methoxy PEG (mPEG) (MW 5.0 kDa), 3-(4,5-Dimethylthiazol-2-yl)-2,5-diphenyltetrazolium bromide (MTT), GSH, 2′,7′-Dichlorodihydrofluorescein diacetate (DCFH-DA), RPMI-1640 medium, 1,3-diphenylisobenzofuran (DPBF) and D_2O (99.9 atom % D) were purchased from Sigma-Aldrich (USA). 5,5′-dithiobis (2-nitrobenzoic acid) (DTNB) was purchased from Fluorochem (UK). Fetal bovine serum (FBS) was obtained from Hyclone (USA). Hoechst 33342 was purchased from Invitrogen. JC-1 assay kit was purchased from MedChemExpress (USA). BODIPY ™ 581/591 C11 was obtained from Thermo Fisher Scientific (USA). Anti-Ki67 antibodies (no. ab15580) and Anti-Glutathione peroxidase 4 (GPX4) antibodies (no. ab125066) were obtained Abcam. Deionized water was produced from Milli-Q Synthesis (18 MΩ, Millipore). All other chemicals were reagent grade and used as received. CT26 cells (murine colon adenocarcinoma cell line) and 4 T1 cells (murine breast cancer cell line) were acquired from Food Industry Research and Development Institute (Hsinchu City, Taiwan).

2.2. Synthesis and characterization of PEG-CS conjugates

PEG-CHO employed in this study was synthesized according to our previous report [46,47]. The detailed synthetic route of PEG-CS conjugates is presented in Fig. 1a. Chitosan (200 mg) and mPEG-CHO (120 mg) were dissolved in anhydrous DMSO (5.0 mL) and the reaction was carried out under stirring at room temperature for 24 h, followed by dialysis (Cellu Sep MWCO 6000–8000) against pH 8.0 phosphate buffer to eliminate unreacted mPEG-CHO and chitosan. The final product was collected by freeze drying and characterized by FT-IR (HORIBA FT-720) and ^{1}H NMR (Agilent DD2 600 MHz NMR spectrometer).

2.3. Preparation of ICG@PEG-CS/PDA NPS

PEG-CS conjugates (1.4 fold with respect to weight of DA residues in feed) dissolved in 0.2 M Tris buffer was added into DA-containing co-solvent (3.5 mg/mL) comprising ethanol and deionized water of 4:3 (*v*/v). The polymerization reaction of DA was performed in dark at room

temperature for 24 h to attain hybrid PEG-CS/PDA nanoparticles. Afterward, the hybrid nanoparticle solution was dialyzed (Cellu Sep MWCO 12000–14,000) against pH 8.0 phosphate buffer at 4 °C to remove unreacted DA, PEG-CS and ethanol. For comparisons, the PDA nanoparticles were prepared in a similar manner. The ICG@PEG-CS/PDA NPS were prepared as follows: ICG dissolved in DMSO (4.0 mg/mL, 0.1 mL) was added dropwise into pH 8.0 phosphate buffer containing PEG-CS/PDA nanoparticles (4.2 mg/mL, 1.9 mL) under stirring. The obtained solution was then stirred in dark at room temperature for 24 h, followed by dialysis (Cellu Sep MWCO 12000–14,000) with pH 8.0 phosphate buffer at 4 °C to remove unloaded ICG molecules and DMSO.

2.4. Characterization of PDA-based nanoparticles

The absorption spectra of DA molecules, PDA nanoparticles, PEG-CS/PDA nanoparticles, free ICG molecules, ICG@PEG-CS/PDA NPS and ICG@PDA NPS in pH 7.4 phosphate buffered saline (PBS) were obtained using a UV/Vis spectrophotometer (U2900, Hitachi, Japan). X-ray photoelectron spectroscopy (XPS) analysis of PDA nanoparticles, PEG-CS conjugates and PEG-CS/PDA nanoparticles was conducted by a PHI 5000 VersaProbe III X-ray photoelectron spectrometer (ULVAC-PHI, Japan) with AlKα radiation (hγ = 1486.6 eV) at 15 kV and 150 W. Thermogravimetric analysis (TGA) was performed with Exstar TG/DTA 6200 (SEIKO INSTRUMENTS Inc.) in a N_2 atmosphere by heating the sample to 900 °C at the rate of 10 °C/min. The particle size and size distribution of various PDA-based nanoparticles in aqueous solutions of different pH values were determined by dynamic light scattering (DLS) using a Brookhaven BI-200SM goniometer equipped with a BI-9000 AT digital correlator using a solid-state laser (35 mW, λ = 637 nm) detected at a scattering angle of 90°. At least triplicate measurements of each sample were conducted and then averaged. To further explore the morphology of PEG-CS/PDA nanoparticles and ICG@PEG-CS/PDA NPS in aqueous solutions at pH 7.4 and 5.0, respectively, in addition to the angular dependence of the autocorrelation functions, the ratio of the root-mean-square radius of gyration (R_g) to the mean hydrodynamic radius (R_h) of these nanoparticles was obtained by angular dependent dynamic and static light scattering (DLS/SLS) measurements using the aforementioned instrument. The R_g of PEG-CS/PDA nanoparticles and ICG@PEG-CS/PDA NPS was quantitatively determined using Berry plot of the scattering intensity ($I_{ex}^{-1/2}$) versus the square of the scattering vector (q^2) from the angle-dependent measurements of the light scattering intensity. The zeta potential of PDA nanoparticles and PEG-CS/PDA nanoparticles with or without ICG payloads in aqueous solutions at different pH was measured with a Litesizer 500 (Anton Paar, USA). The morphology of PEG-CS/PDA nanoparticles with or without ICG payloads was acquired by transmission electron microscope (TEM) (JEM-1400 FLASH, JEOL, Japan) and scanning electron microscope (SEM) (JEOL JSM-7800F Prime Schottky Field Emission SEM, Japan).

To quantify ICG encapsulated within nanoparticles, 100 μL of the purified ICG@PEG-CS/PDA NPS solution was lyophilized and then dispersed in DMSO for complete drug isolation from nanoparticles. Afterward, the solution was centrifuged at 15000 rpm to collect the supernatant for analysis. The absorbance of ICG at 794 nm was measured by UV/Vis spectrophotometer (U-2900, Hitachi). The calibration curve utilized for ICG loading assessment was established by absorbance of ICG with various concentrations in DMSO. The ICG loading efficiency (LE) and loading content (LC) were calculated by the following formulas:

$$\text{LE}\ (\%) = (\text{weight of loaded ICG}/\text{weight of ICG in feed}) \times 100\%.$$

$$\text{LC}\ (\%) = (\text{weight of loaded ICG}/\text{total weight of ICG} - \text{carrying NPS}) \times 100\%.$$

To explore the aqueous photo-stability of ICG, the characteristic ICG absorbance of free ICG molecules and ICG@PEG-CS/PDA NPS (ICG concentration = 23 μM) in pH 7.4 PBS at 37 °C was determined over time by UV/Vis spectrophotometer (U-2900, Hitachi). The ICG absorbance measured at different time intervals was normalized by the following formula.

$$\text{Normalized absorbance}\ (\%) = (\text{ICG absorbance at the predetermined time points}/\text{initial ICG absorbance}) \times 100\%.$$

For in vitro ICG release test, the ICG@PEG-CS/PDA nanoparticle dispersion (1.0 mL) was dialyzed (Cellu Sep MWCO 12000–14,000) against PBS (pH 7.4 or 6.5) and acetate buffer (pH 5.0) (20 mL) at 37 °C, respectively. At prescribed time intervals, the internal sample was withdrawn periodically for measurement of maximum ICG absorbance by the UV/Vis spectrophotometer (U2900, Hitachi, Japan). After each analysis, the sample was then put back into the dialysis bag. The cumulative ICG release (%) was obtained by the following formula:

$$\text{Cumulative ICG release}\ (\%) = ((A_o - A_t/A_o) \times 100\%.$$

A_o = Initial ICG absorbance
A_t = ICG absorbance at different time points

2.5. Photothermal conversion effect and stability

Free ICG molecules, PEG-CS/PDA nanoparticles, ICG@/PDA NPS and ICG@PEG-CS/PDA NPS dispersed in pH 7.4 PBS (1.0 mL), respectively, were irradiated by 808 nm NIR laser (1.0 W/cm^2) for 5 min. The solution temperatures and infrared thermographic maps were recorded with an infrared thermal imaging camera (Thermo Shot F20, NEC Avio Infrared Technologies, Germany). Also, according to the data from the cooling status, the PCE (η) of the above formulations was calculated by the previously reported formula [47]. Moreover, the temperature of an aqueous solution containing ICG@PEG-CS/PDA NPS of different concentrations exposed to laser irradiation (1.0 W/cm^2) for 5 min was monitored by the above apparatus. On the other hand, to evaluate the photothermal stability, an aqueous solution of free ICG molecules (42.5 μM), PEG-CS/PDA nanoparticles (200 μg/mL) and ICG@PEG-CS/PDA NPS (ICG concentration = 42.5 μM) was irradiated with 808 nm laser (1.0 W/cm^2) for 2.5-min laser on and 5-min laser off cycles. Furthermore, the ICG absorbance of free ICG molecule and ICG@PEG-CS/PDA nanoparticle solutions (ICG concentration = 42.5 μM) receiving various on/off cycles of laser irradiation was determined by UV/Vis spectrophotometer. The ICG absorbance measured at different on/off cycles of laser irradiation was normalized by the following formula.

$$\text{Normalized absorbance}\ (\%) = (\text{ICG absorbance at various on/off cycles of laser irradiation}/\text{initial ICG absorbance}) \times 100\%.$$

On the other hand, the particle size of PEG-CS/PDA nanoparticles and ICG@PEG-CS/PDA NPS with or without NIR laser irradiation was attained by DLS measurement.

2.6. Singlet oxygen generation and GSH depletion

The NIR-activated singlet oxygen generation of free ICG molecules and ICG@PEG-CS/PDA NPS dispersed in pH 7.4 PBS was evaluated by DPBF assay. Briefly, free ICG molecules and ICG@PEG-CS/PDA NPS (ICG concentration = 65 μM) were dispersed in DPBF solution (225 μg/mL) containing GSH (100 μM) or not and the aqueous solutions were irradiated with 808 nm laser (1.0 W/cm^2) for 2.5, 5.0 and 10 min. The absorption spectra of DPBF were recorded by UV/Vis spectrophotometer. The normalized DPBF absorbance was calculated by the following formula.

Normalized absorbance (%) = (DPBF absorbance after different laser irradiation times/initial DPBF absorbance) × 100%.

The GSH depleting capability of PEG-CS/PDA nanoparticles with or without ICG loading was studied by DTNB assay. Briefly, the PEG-CS/PDA nanoparticles (400 μg/mL) and ICG@PEG-CS/PDA nanozymes (400 μg/mL) were respectively added to 1 mL of GSH solution (100 μM) and reacted at 37 °C for 2, 4, 8 and 24 h. Next, the resulting solution was centrifugated at 16000 rpm for 10 min to collect the supernatant. Then, 250 μL of DTNB (100 μM) was added to the supernatant and the absorbance of the mixture at 412 nm was examined. Furthermore, at the prescribed 2 h reaction time, the GSH depleting capability of the PEG-CS/PDA nanoparticles and ICG@PEG-CS/PDA NPS at 37 and 50 °C was assessed by the similar manner.

2.7. In vitro cellular uptake

CT26 cells (2 × 10^5 cells/well) seeded in 6-well plates were incubated with free ICG molecules and ICG@PEG-CS/PDA NPS (ICG concentration = 5 μM), respectively, for 1 and 4 h at 37 °C. After being detached with trypsin-EDTA solution, the ICG fluorescence signals of the treated CT26 cells suspended in PBS (1.0 mL) were analyzed by the FACSCalibur flow cytometer (BD Bioscience). On the other hand, CT26 cells (2 × 10^5 cells/well) seeded onto 22 mm round glass coverslips in 6-well plates were incubated with free ICG molecules and ICG@PEG-CS/PDA NPS (ICG concentration = 5 μM), respectively, for 1 and 4 h at 37 °C. After being washed three times with Hanks' balanced salt solution (HBSS) and immobilized with 4 % formaldehyde, the cell nuclei were stained with Hoechst 33342. The cellular images were gained by confocal laser scanning microscope (CLSM) (Olympus, FluoView FV3000, Japan) at the excitation wavelengths of 405 and 782 nm for Hoechst and ICG, respectively.

2.8. Intracellular GSH depletion and singlet oxygen generation

To evaluate intracellular GSH consumption, CT26 cells (1.5 × 10^5/well) seeded in 6-well plate were incubated with free ICG molecules (12 μM), PEG-CS/PDA nanoparticles (100 or 200 μg/mL) and ICG@PEG-CS/PDA NPS (200 μg/mL), respectively, for 24 h. After being washed twice with PBS, the treated cells were detached with trypsin-EDTA and then centrifugated (1500 rpm) for 5 min. The collected cell pellets were irradiated by 808 nm NIR laser (1.0 W/cm^2) for 5 min and re-dispersed in 0.3 mL RIPA buffer, followed by freezing and thawing for cell lysis. After being centrifuged at 12000 rpm for 10 min at 25 °C, the supernatant was taken out and intracellular GSH level of each group was determined by DTNB-thiol assay kit through a microplate reader at a wavelength of 405 nm. The intracellular GSH level of CT26 cells treated with the above formulations without laser irradiation was also assessed in a similar manner.

On the other hand, to explore the intracellular singlet oxygen generation, CT26 cells (2 × 10^5 cells/well) seeded onto 22 mm round glass coverslips in 6-well plates were incubated with PEG-CS/PDA nanoparticles (360 μg/mL), free ICG molecules or ICG@PEG-CS/PDA NPS (ICG concentration = 20 μM) at 37 °C for 4 h. After discarding the culture medium, the cells were irradiated with 808 nm NIR laser (1.0 W/cm^2) for 10 min. Afterward, the cells were treated with DCFH-DA (10 μM) for 30 min and washed three times with HBSS, followed by immobilization with 4 % formaldehyde. The cellular images were attained using CLSM (Olympus, FluoView FV3000, Japan) at excitation wavelengths of 485 nm for DCF.

2.9. Mitochondrial membrane potential (MMP) analysis

The MMP detection kit (JC-1) was to observe the depolarization of the mitochondria membranes. CT26 cells (2 × 10^5/well) seeded in 6-well plate were incubated with PEG-CS/PDA nanoparticles (360 μg/mL), free ICG molecules and ICG@PEG-CS/PDA NPS (ICG concentration = 20 μM), respectively, for 4 h. After discarding the culture medium, the cells were irradiated with 808 nm NIR laser (1.0 W/cm^2) for 10 min. Subsequently, the cells were incubated with JC-1 (2 μM) for 30 min and washed two times with HBSS, followed by immobilization with 4 % formaldehyde. The cellular images were acquired using fluorescence microscopy (ZEISS Axio Imager M2) at excitation wavelengths of 485 and 535 nm for JC-1 monomer and JC-1 aggregate, respectively.

2.10. Intracellular lipid peroxide examination.

CT26 cells (2 × 10^5/well) seeded in 6-well plate were incubated with PEG-CS/PDA nanoparticles (360 mg/mL), free ICG molecules and ICG@PEG-CS/PDA NPS (ICG concentration = 20 μM), respectively, for 4 h. After discarding the culture medium, the cells were irradiated with 808 nm NIR laser (1.0 W/cm^2) for 10 min. Subsequently, the cells were incubated with BODIPY™ 581/591 C11 (5 μM) for 30 min and washed two times with HBSS, followed by immobilization with 4 % formaldehyde. Finally, the intracellular lipoperoxidation was observed by fluorescence microscopy (ZEISS Axio Imager M2).

2.11. In Vitro PDT/PTT anticancer efficacy

CT26 cells (1.5 × 10^5 cells/well) seeded in a 6-well plate were incubated at 37 °C for 24 h in RPMI-1640 containing 10 % FBS and 1 % penicillin. The medium was then replaced with 1.0 mL of fresh medium containing free ICG molecules, PEG-CS/PDA nanoparticles or ICG@PEG-CS/PDA NPS of different concentrations and incubated for additional 24 h. After being washed twice with PBS, cells were detached with trypsin-EDTA and centrifuged (1500 rpm). After removal of supernatant, the collected cell pellets were irradiated with NIR 808 nm laser (1.0 W/cm^2) for 2 min. The laser-treated cells dispersed in 0.85 mL fresh medium were reseeded in a 12-well plate and incubated for additional 24 h. MTT (0.25 mg/mL, 1.0 mL) was then added into each well, followed by incubation at 37 °C for 3 h. After discarding the culture medium, DMSO (0.8 mL) was added to dissolve the precipitate and the

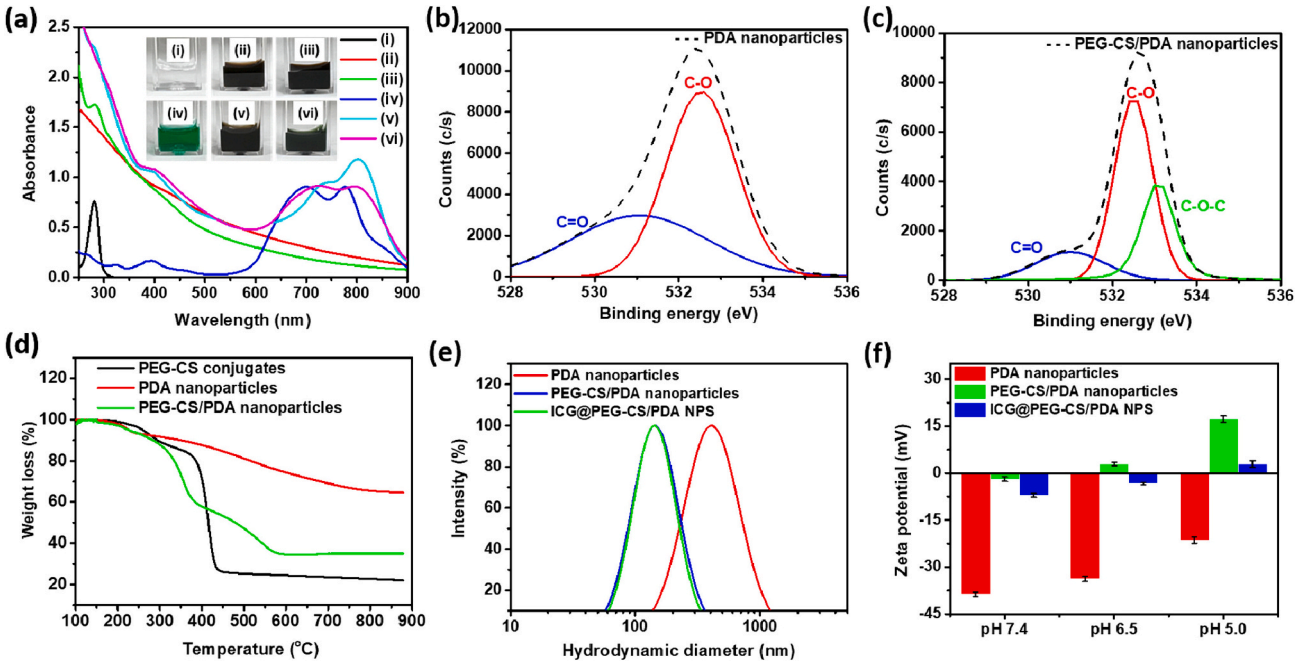

Fig. 2. (a) UV/Vis spectra of aqueous solutions of (i) DA molecules, (ii) PDA nanoparticles, (iii) PEG-CS/PDA nanoparticles, (iv) free ICG molecules, (v) ICG@PEG-CS/PDA NPS and (vi) ICG@PDA NPS. O1s XPS spectra of (b) PDA nanoparticles and (c) PEG-CS/PDA nanoparticles. (d) TGA profiles of PEG-CS conjugates, PDA nanoparticles and PEG-CS/PDA nanoparticles. (e) DLS particle size distribution profiles of PDA nanoparticles, PEG-CS/PDA nanoparticles and ICG@PEG-CS/PDA NPS in pH 7.4 PBS. (f) Zeta potential of various PDA-containing nanoparticles in aqueous solutions of pH 7.4, 6.5 and 5.0.

absorbance of the resulting solution at 570 nm was measured by a BioTek 800TS microplate reader. The cell viability of CT26 cells treated with free ICG molecules, PEG-CS/PDA nanoparticles or ICG@PEG-CS/PDA NPS in the absence of NIR laser irradiation was also assessed in a similar approach. Besides, the PDT/PTT-mediated anticancer effect of ICG@PEG-CS/PDA NPS on 4 T1 cells was evaluated by the similar manner.

2.12. Live and dead cell assay

CT26 cells (2.0×10^5 cells/well) seeded in a 12-well plate were incubated at 37 °C for 24 h in RPMI-1640 containing 10 % FBS and 1 % penicillin. The medium was then replaced with 1.0 mL of fresh medium containing free ICG molecules (1.25 μM), PEG-CS/PDA nanoparticles (22.5 μg/mL) or ICG@PEG-CS/PDA NPS (ICG concentration = 1.25 μM; PEG-CS/PDA nanoparticle concentration = 22.5 μg/mL) and incubated for additional 24 h. After that, cells were irradiated with 808 nm NIR laser (1.0 W/cm^2) for 2 min and gently washed with HBSS twice to avoid washing off dead cells. Calcein AM (2 μg/mL) and propidium iodide (PI, 4 μg/mL) mixture solution (500 μL) was added and kept at room temperature for 45 min. The cellular images were obtained with a NIB-100F inverted fluorescent biological microscope (Nanjing Jiangnan Novel Optics Co., Ltd., China)

2.13. Animals and tumor model

Healthy female BALB/c mice (5–7 weeks old, 20 ± 2 g) purchased from National Laboratory Animal Center (Taiwan) were cared in accordance with the Guidance Suggestions for the Care and Use of Laboratory Animals, approved by the Administrative Committee on Animal Research in the Chung Shan Medical University (Taiwan) (IACUC Approval No: 2722). Meanwhile, animal experiments also complied with the National Research Council's Guide for the Care and Use of Laboratory Animals. The animals were housed in standard environmental conditions, i.e., pathogen-free area, at a temperature of 25 ± 0.5°C, with provision of standard diet and water excess. To establish tumor model, 5×10^6 CT26 cells were subcutaneously injected into the right thigh of mice. After 10 days post-inoculation, the tumor model was attained. Tumor volume (V) was calculated as follows: $V = L \times W^2/2$, where W is the tumor measurement at the widest point and L the tumor dimension at the longest point.

2.14. In vivo imaging and biodistribution

When the tumor volume reached 90–120 mm^3, all mice were randomly allocated into 3 groups (n = 1 in PBS group, n = 3 in free ICG and ICG@PEG-CS/PDA NPS groups, respectively) and injected intratumorally with 100 μL of PBS, free ICG or ICG@PEG-CS/PDA NPS at a dosage of 0.1 mg/kg ICG. The fluorescence signals of ICG (Ex. 710 nm and Em. 760 nm) at 0.5, 6, 24 and 48 h post-injection were collected using an IVIS imaging system (IVIS Lumina II, Caliper, LifeSciences, MA, USA). The treated mice were sacrificed at 48 h post-injection and the major organs and tumor were harvested for individual organ imaging by IVIS.

2.15. In vivo NIR-triggered tumor hyperthermia

When tumor volume of mice reached 90–120 mm^3, mice were randomly divided into 4 groups (n = 4 in each group) and injected intratumorally with 100 μL of PBS, PEG-CS/PDA nanoparticles, free ICG molecules or ICG@PEG-CS/PDA NPS at an ICG dosage of 0.1 mg/kg or, in the case of PEG-CS/PDA nanoparticles, 2.2 mg PEG-CS/PDA nanoparticles/kg. At 0.5 h post-injection, the tumor region of mice was irradiated by the 808 nm laser with a power density of 1.0 W/cm^2 for 2 min. The infrared thermographic maps of mice and the tumor local temperature during NIR laser irradiation were attained with infrared thermal imaging camera (Thermo Shot F20, NEC Avio Infrared Technologies, Germany).

2.16. In vivo tumor growth inhibition

When tumor volume of mice reached 90–120 mm^3, mice were

Table 1
DLS data and ICG loading characteristics of PDA-based nanoparticles.

Sample	D_h (nm)	PDI	LE (%)	LC (wt%)
PDA nanoparticles	431.7 ± 20.6	0.296	–	–
PEG-CS/PDA nanoparticles	142.5 ± 5.3	0.184	–	–
ICG@PDA NPS	143.3 ± 14.3	0.173	67.7 ± 1.8	8.74 ± 0.21
ICG@PEG-CS/PDA NPS	143.2 ± 6.8	0.217	96.4 ± 2.6	4.60 ± 0.12

randomly divided into 5 groups (n = 4 in each group) and injected intratumorally with 100 μL of PBS, PEG-CS/PDA nanoparticles, free ICG molecules or ICG@PEG-CS/PDA NPS at an ICG dosage of 0.1 mg/kg or, in the case of PEG-CS/PDA nanoparticles, 2.2 mg PEG-CS/PDA nanoparticles/kg. At 0.5 h and one day post-injection, the tumor region of mice was irradiated by the 808 nm laser with a power density of 1.0 W/cm^2 for 2 min. The tumor volumes and body weight of various groups were measured every two days until 14 days post-injection. Tumor sections of pertinent sizes were stained with H&E, anti-Ki67 antibodies and anti-GPX4 antibodies, respectively, and observed by digital microscope. Furthermore, sections of major organs were stained with H&E and observed by the above instrument.

2.17. Statistical analysis

Data are reported as mean ± SD. The differences among groups were determined using one-way or two-way ANOVA analysis; ns > 0.05, *p < 0.05, **p < 0.01, ***p < 0.001. All statistical analyses were performed using Prism software. (PRISM 5.01 GraphPad Software).

3. Results and discussion

3.1. Synthesis and characterization of PEG-CS conjugates

Through Schiff base reaction of mPEG-CHO and chitosan (Fig. 1a), the PEG-CS conjugates were attained and used in the preparation of PEG-CS/PDA nanoparticles. As shown in the FT-IR spectrum of PEG-CS conjugates (Fig. S1), in addition to the feature bands of C—O and C═N stretching vibration from ethylene glycol residues and imine linkages at 1145 and 1649 cm^{-1}, respectively, the absorption band of the N—H and O—H stretching vibration from chitosan at 3200–3600 cm^{-1} was observed. Furthermore, in addition to the absence of the proton signals of aldehyde groups at δ 10.1 ppm, the feature proton signals of ethylene groups of mPEG at δ 3.7 ppm, and of benzene ring group at δ 7.9–8.2 ppm were observed in the ^{1}H NMR spectrum of PEC-CS conjugates (Fig. 1b). These findings confirm the successful conjugation of chitosan with mPEG-CHO upon the formation of benzoic imine bonds. According to the signal integral ratio of the methoxy protons (δ 3.4 ppm) of mPEG-CHO and the H2 protons (δ 2.7 ppm) from glucosamine groups of chitosan, the degree of substitution of chitosan with mPEG-CHO defined here as the number of mPEG segments per 100 glucosamine units was attained to be ca 11.1.

3.2. Preparation and characterization of ICG@PEG-CS/PDA NPS

To obtain PEG-CS/PDA nanoparticles as ICG vehicles, the self-polymerization of DA molecules was performed in Tris buffer containing PEG-CS conjugates. As shown in Fig. 2a, the resulting PEG-CS/PDA nanoparticles exhibited the enhanced absorption from 300 to 800 nm, whereas the DA molecules displayed feature absorption peak at 281 nm. Also, compared to DA solution with colorless and transparent state, the PEG-CS/PDA nanoparticle solution displayed a dark black hue. Undoubtedly, through simple one-step co-deposition of DA molecules and PEG-CS conjugates, the hybrid PEG-CS/PDA nanoparticles were successfully attained. As revealed in the XPS spectra (Fig. 2b and c and S2), the PEG-CS/PDA nanoparticles possessed the characteristic peak of C-O-C (533.0 eV) from PEG-CS conjugates and the peaks of C═O (531.0 eV) and C—O (532.5 eV) from PDA nanoparticles. Furthermore, in addition to the feature peaks of pyridinc N (398.3 eV), pyrrolic N (399.5 eV) and graphitic N (400.4 eV) from PDA nanoparticles, the new peaks of amine (399.4 eV) and amide (399.7 eV) from PEG-CS conjugates were attained for hybrid PEG-CS/PDA nanoparticles (Fig. S3). These results clearly confirm the effective coupling of PEG-CS conjugates with PDA nanoparticles upon Michael addition between primary amine groups of

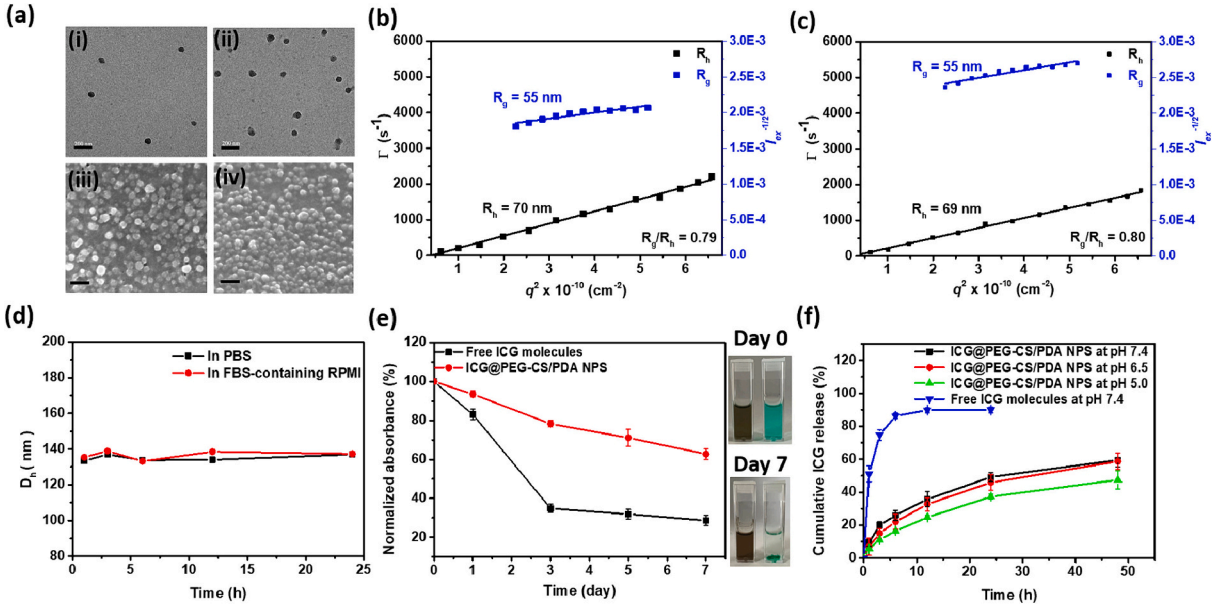

Fig. 3. (a) TEM images of (i) PEG-CS/PDA nanoparticles and (ii) ICG@PEG-CS/PDA NPS. SEM images of (iii) PEG-CS/PDA nanoparticles and (iv) ICG@PEG-CS/PDA NPS. Scale bars are 200 nm. Berry plot for R_g and angle dependent correlation function of R_h of (b) PEG-CS/PDA nanoparticles and (c) ICG@PEG-CS/PDA NPS in pH 7.4 0.15 M PBS. (d) Time-evolved mean hydrodynamic diameter of ICG@PEG-CS/PDA NPS dispersed in pH 7.4 PBS and FBS-containing RPMI-1640. (e) Normalized maximum absorbance of free ICG molecules and ICG@PEG-CS/PDA NPS (ICG concentration = 23 μM) in pH 7.4 0.15 M PBS at 37 °C. Inset: photographs of aqueous solutions containing free ICG molecules (right) or ICG@PEG-CS/PDA NPS (left) on day 0 and 7. (f) Cumulative ICG release profiles of ICG@PEG-CS/PDA NPS in aqueous solutions of pH 7.4, 6.5 and 5.0 at 37 °C. For comparison, diffusion of free ICG molecules across the dialysis tube at pH 7.4 is included.

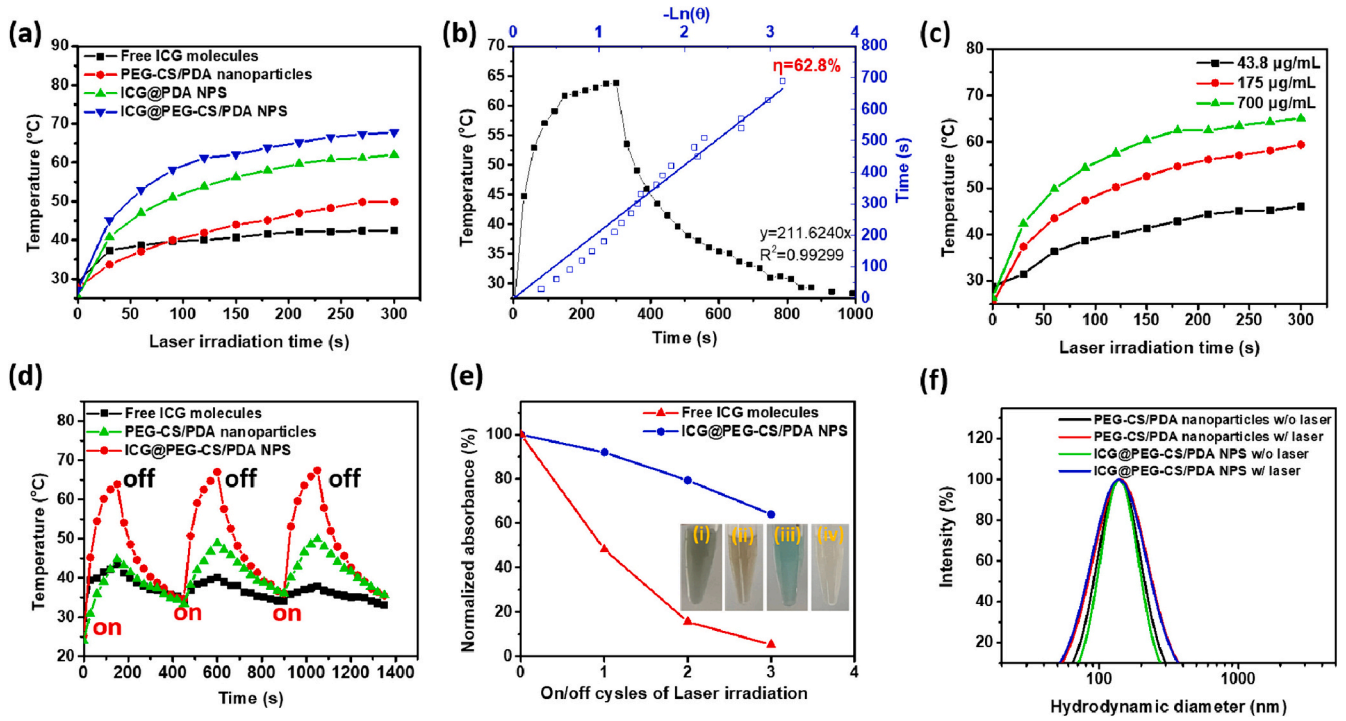

Fig. 4. (a) Temperature profiles of free ICG molecules, ICG@PDA NPS, PEG-CS/PDA nanoparticles and ICG@PEG-CS/PDA NPS (ICG concentration: 42.5 μM, PDA concentration: 200 μg/mL) in pH 7.4 phosphate buffer with 808 nm NIR laser irradiation (1.0 W/cm^2). (b) Temperature profile of ICG@PEG-CS/PDA nanoparticle solution (ICG concentration: 42.5 μM, PDA concentration: 200 μg/mL) after exposure to 808 nm laser irradiation (1.0 W/cm^2) for single on/off cycle of laser irradiation, and plot of cooling time versus negative logarithm of the temperature driving force. (c) Temperature change of aqueous solutions containing ICG@PEG-CS/PDA NPS of different concentrations under NIR laser irradiation (1.0 W/cm^2). (d) Temperature change of aqueous solutions containing free ICG molecules, PEG-CS/PDA nanoparticles or ICG@PEG-CS/PDA NPS (ICG concentration: 42.5 μM, PDA concentration: 200 μg/mL) exposed to three on/off cycles of 808 nm NIR laser irradiation (1.0 W/cm^2). (e) Normalized absorbance of free ICG molecules and ICG@PEG-CS/PDA NPS in pH 7.4 PBS exposed to various on/off cycles of laser irradiation. Inset: photographs of ICG@PEG-CS/PDA NPS and free ICG molecule solution before (i, iii) and after (ii, iv) three on/off cycles of laser irradiation. (f) DLS particle size distribution profiles of PEG-CS/PDA nanoparticles and ICG@PEG-CS/PDA NPS in aqueous solutions with or without NIR laser irradiation (1.0 W/cm^2, 2 min).

chitosan with 5,6-dihydroxyindole units of PDA (Scheme 1a). According to the TGA profiles shown in Fig. 2d, the PEG-CS/PDA nanoparticles consist of approximately 64.7 wt% PEG-CS and 35.3 wt% PDA.

The mean hydrodynamic diameters and polydispersity index of PEG-CS/PDA nanoparticles in pH 7.4 PBS characterized by DLS were ca 142.5 nm and 0.184, respectively, (Fig. 2e and Table 1). By contrast, the PDA nanoparticles from self-polymerization of DA monomers alone exhibited appreciably large particle size (ca 431.7 nm) after being dispersed in PBS, being attributed to the inter-particle aggregation as evidenced by their TEM images (Fig. S4). As presented in Fig. 2f, the PEG-CS/PDA nanoparticles at pH 7.4 displayed a zeta potential absolute value of ca −1.9 mV significantly lower than the PDA nanoparticles (ca −38.7 mV). This signifies that the hydrophilic PEG-CS conjugates covalently decorated on the surfaces of PDA nanoparticles could remarkably shield the negatively-charged phenolic hydroxyl groups of PDA cores. Moreover, with the solution pH being reduced from 7.4 to 5.0, the zeta potential of PDA nanoparticles was changed from −38.7 to −21.4 mV due to the declined dissociation of phenolic hydroxyl groups [38,48], while the conversions in zeta potential of PEG-CS/PDA nanoparticles from nearly neutral (−1.9 mV) to positive values (+17.3 mV) were obtained because of the decreased dissociation of phenolic hydroxyl groups as well as increased protonation of primary amine groups from chitosan segments. Importantly, taking advantage of the excellent hydration and steric repulsion effect of PEG-CS-rich surfaces, the PEG-CS/PDA nanoparticles dispersed in pH 7.4 PBS still maintained sound colloidal stability over 24 h as shown in Fig. S5.

TEM and SEM images of PEG-CS/PDA nanoparticles clearly illustrate their well-dispersed spherical shape (Fig. 3a). Also, based on a high linear correlation between the relaxation frequency (Γ) and the square of the scattering vector (q^2) from the angle-dependent DLS data of PEG-CS/PDA nanoparticles in PBS (Fig. 3b), these nanoparticles were characterized to possess a spherical form in aqueous solution. Furthermore, the R_g of PEG-CS/PDA nanoparticles was examined by angle-dependent SLS to be ca 55 nm (Fig. 3b). For PEG-CS/PDA nanoparticles, the calculated R_g/R_h value (ca 0.79) is comparable to that (0.78) of solid sphere-like nanoparticles [49,50]. According to the above results, the PEG-CS/PDA nanoparticles were demonstrated to have a spherical architecture comprising hydrophobic PDA core and hydrophilic PEG-CS shell (Scheme 1a).

To obtain the ICG@PEG-CS/PDA NPS, ICG molecules were added into aqueous solution of PEG-CS/PDA nanoparticles and then stirred for 24 h. For comparison, the ICG@PDA NPS were also prepared in a similar way. As presented in the UV/Vis spectra (Fig. 2a), compared to free ICG molecules, the ICG@PDA NPS and ICG@PEG-CS/PDA NPS showed remarkable red shift of characteristic ICG absorption peak from 775 to 795 and 804 nm, respectively, indicating the successful ICG loading. Similar results regarding the UV/Vis spectrum of free ICG molecules in aqueous solution and the red shift of absorption peak of ICG encapsulated within PDA-containing nanoparticles were also reported elsewhere [20,51–55]. Moreover, the particle size and size distribution ICG@PEG-CS/PDA NPS were comparable to those of drug-free PEG-CS/PDA nanoparticles (Fig. 2e and Table 1). The zeta potential of PEG-CS/PDA nanoparticles after being loaded with ICG molecules was converted from −1.9 to −7.1 mV (Fig. 2f), implying attachment of ICG molecules on the particle surfaces to expose their negatively-charged sulfonate groups. Importantly, the ICG@PEG-CS/PDA NPS showed profound drug loading efficiency and content for 96.4 % and 4.6 wt% (Table 1). By contrast, in the lack of PEG-CS coating, the ICG@PDA NPS had a low ICG

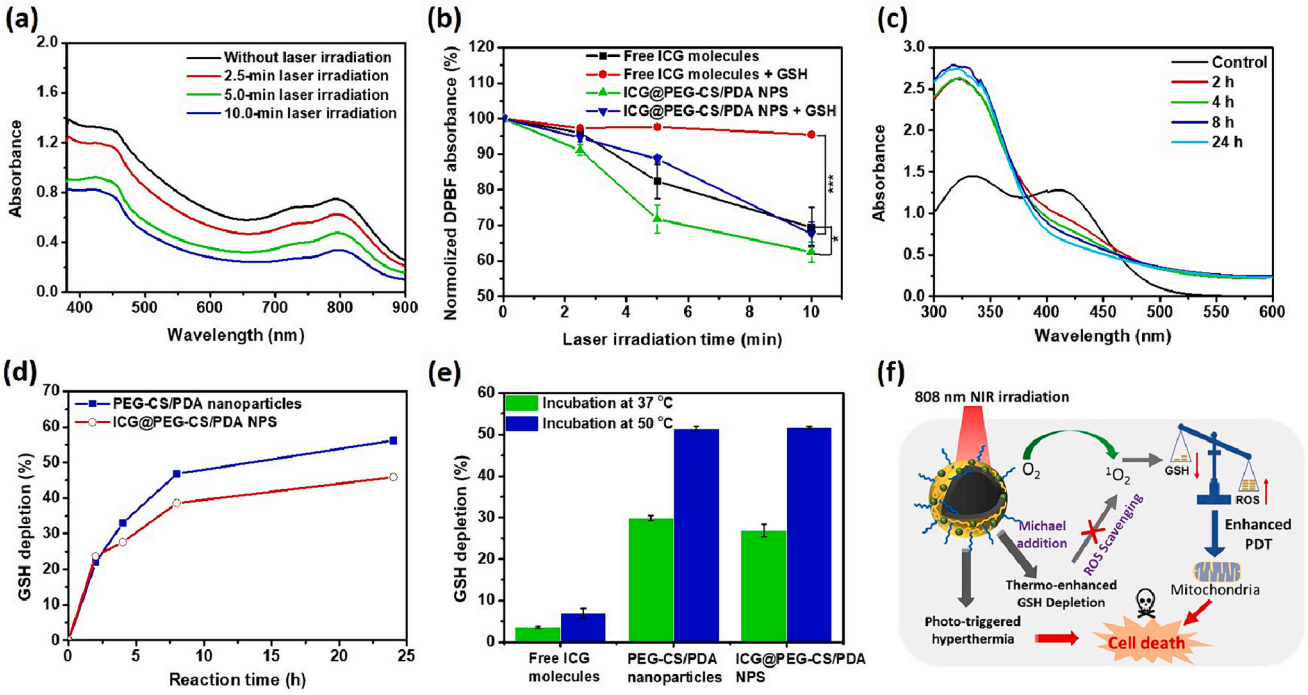

Fig. 5. (a) UV/Vis spectra of DPBF molecules in ICG@PEG-CS/PDA nanoparticle solution exposed to 808 nm NIR laser irradiation (1.0 W/cm^2). (b) Normalized absorbance of DPBF molecules in aqueous solutions containing free ICG molecules and ICG@PEG-CS/PDA NPS, respectively, with or without addition of 100 μM GSH, exposed to NIR laser irradiation (1.0 W/cm^2). (c) UV/Vis spectra of DTNB molecules dissolved in GSH solution pretreated with ICG@PEG-CS/PDA NPS at 37 °C for various time intervals. (d) Time-evolved cumulative GSH depletion of PEG-CS/PDA nanoparticles and ICG@PEG-CS/PDA NPS at 37 °C. (e) Cumulative GSH depletion of PEG-CS/PDA nanoparticles and ICG@PEG-CS/PDA NPS at 37 and 50 °C for 4 h. (f) Schematic illustration of the augmented PDT/PTT anticancer effect of ICG@PEG-CS/PDA NPS exposed to NIR laser irradiation.

loading efficiency (67.7 %). The above results further demonstrate that the electrostatic attraction of sulfonate-bearing ICG molecules and amine-rich PEG-CS layers in combination with the π-π stacking and hydrophobic interactions between ICG and PDA could effectively promote the integration of ICG molecules with PEG-CS/PDA nanoparticles.

Based on the TEM and SEM images (Fig. 3a), and angle-dependent DLS and SLS data (Fig. 3c), the ICG@PEG-CS/PDA NPS exhibited well-dispersed spherical solid-like structure. On the other hand, no significant variation in the particle size of ICG@PEG-CS/PDA NPS dispersed in pH 7.4 PBS or FBS-containing RPMI for 24 h was observed (Fig. 3d), suggesting their excellent colloidal stability. As presented in Fig. 3e, different from the considerable reduction in the normalized absorbance of free ICG molecules in PBS at 37 °C over 3 days, the normalized ICG absorbance of ICG@PEG-CS/PDA NPS was slightly decreased under the same condition. Moreover, the ICG@PEG-CS/PDA NPS dispersed in the above environment for 7 days maintained well suspension, whereas ICG molecules tended to aggregate and precipitate. The findings suggest that the ICG@PEG-CS/PDA NPS could not only increase the photostability of ICG molecules but also prevent their aggregation. Note that, different from quick diffusion of free ICG molecules across dialysis tube in pH 7.4 PBS (over 80 % within 6 h) (Fig. 3f), the sustained ICG release from ICG@PEG-CS/PDA NPS at pH 7.4, 6.5 and 5.0 was attained (beyond 40 % during 48 h), being attributed to the attachment of ICG to PEG-CS/PDA nanoparticles by multiple interactions as described above. Moreover, for ICG@PEG-CS/PDA NPS, the total amount of ICG released at pH 5.0 was slightly less compared to that at pH 7.4 and 6.5. This could be ascribed to that the promoted protonation of primary amine groups from PEG-CS layers and reduced dissociation of phenolic hydroxyl groups from PDA nanoparticles at pH 5.0 further enhance the interactions of PEG-CS/PDA nanoparticles with ICG molecules, thereby hindering ICG liberation.

3.3. Photothermal effect and stability of ICG@PEG-CS/PDA NPS

To explore the practicability of ICG@PEG-CS/PDA NPS used in PTT-mediated cancer treatment, their photothermal capability and stability was assessed by measuring temperature variation of aqueous solution containing ICG-loaded NPS under irradiation of 808 nm NIR laser. As revealed in Fig. 4a, during NIR laser irradiation (1.0 W/cm^2 for 300 s), the temperature of ICG@PEG-CS/PDA nanoparticle solution (ICG concentration = 42.5 μM, PDA concentration = 200 μg/mL) was markedly elevated compared to that of aqueous solutions containing either free ICG molecules or PEG-CS/PDA nanoparticles at the same ICG and PDA concentrations. Importantly, based on the photothermal heating-cooling curve (Fig. 4b), the PCE (η) of ICG@PEG-CS/PDA NPS was calculated to be ca 62.8 %, being prominently higher than that of free ICG molecules (ca 15.7 %) and that of PEG-CS/PDA nanoparticles (38.5 %) and that of ICG@PDA NPS (40.9 %) (Fig. S6). Obviously, in addition to π-π stacking and hydrophobic interaction between ICG and PDA, the electrostatic attraction of amine-rich PEG-CS with negatively-charged ICG plays an important role in promoting the incorporation of ICG in monomer rather than dimer form with PEG-CS/PDA nanoparticles, thereby leading to remarkable red shift of ICG absorption as shown in Fig. 2a. Such a red-shifted ICG absorption of ICG@PEG-CS/PDA NPS better approaches the central wavelength (808 nm) of the NIR laser, thus enhancing their absorbing NIR capability and PCE. It should be highlighted that ICG@PEG-CS/PDA NPS exhibited a higher PCE (beyond 60 %) compared to other ICG-loaded PDA-containing nanoparticles (PCE below 48 %) reported in previous works [20,21,42–44]. As expected, when the concentration of ICG@PEG-CS/PDA NPS in aqueous solution was increased from 175 to 700 μg/mL, the NIR-triggered elevation of solution temperature was further promoted (Fig. 4c). More importantly, after three on/off cycles of NIR laser irradiation, the ICG@PEG-CS/PDA NPS still retained virtually intact photothermal capability, while free ICG molecules showed considerably lowered photothermal effect

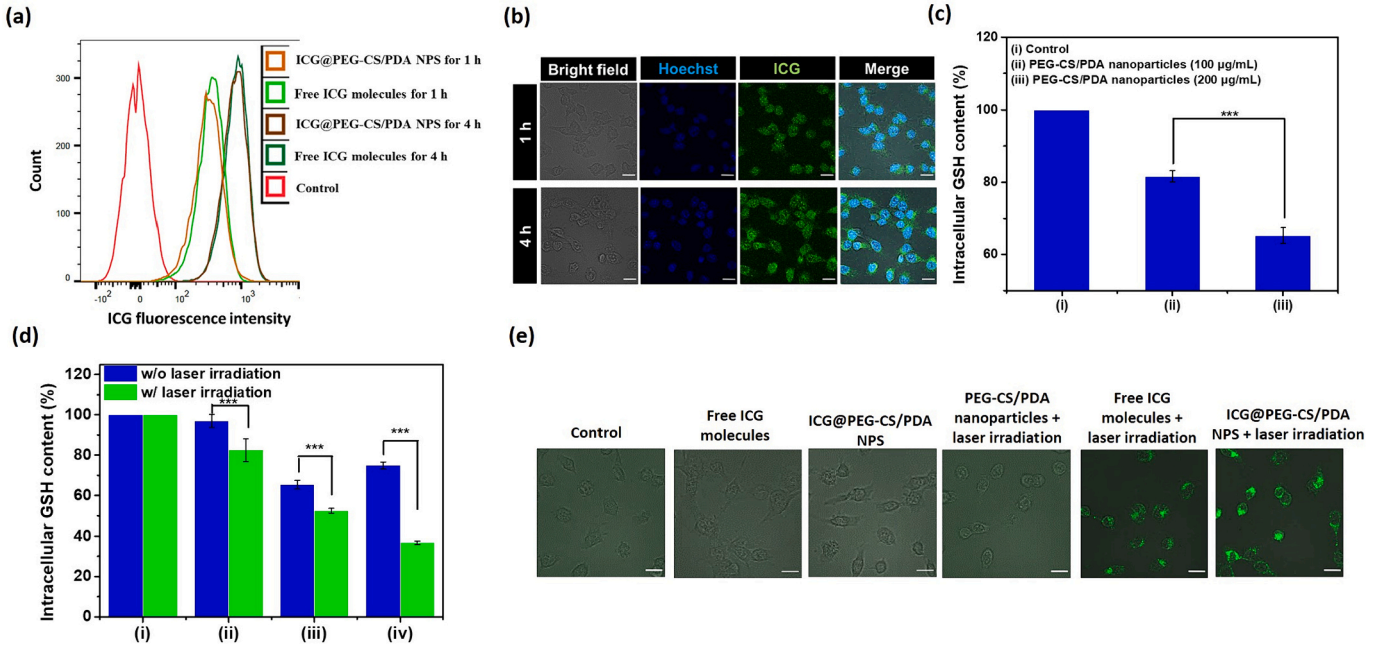

Fig. 6. (a) Flow cytometric histograms (b) CLSM images of CT26 cells incubated with free ICG molecules or ICG@PEG-CS/PDA NPS for 1 and 4 h, respectively, at 37 °C (ICG = 5 μM). Scale bars are 15 μm. (c) Intracellular GSH content of CT26 cells treated with PEG-CS/PDA nanoparticles for 24 h in the lack of NIR laser irradiation. (d) Intracellular GSH content of CT26 cells treated with (i) PBS, (ii) free ICG molecules, (iii) PEG-CS/PDA nanoparticles and (iv) ICG@PEG-CS/PDA NPS, respectively, for 24 h with or without NIR laser irradiation (1.0 W/cm^2, 5 min). (e) DCF fluorescence images of CT26 cells receiving different formulations with or without laser irradiation (1.0 W/cm^2, 10 min). Scale bars are 15 μm. ns > 0.05, *p < 0.05, **p < 0.01, ***p < 0.001.

(Fig. 4d). Also, after three on/off cycles of NIR laser irradiation, the absorbance of free ICG molecules in the wavelength range of 600–850 nm was appreciably reduced in comparison with that of ICG@PEG-CS/PDA NPS (Fig. S7). Compared to the considerable decline in the normalized absorbance of free ICG molecules owing to their severe photo-bleaching, only mild decrease in the normalized absorbance and nearly unchanged particle size were observed for ICG@PEG-CS/PDA NPS (Fig. 4e and f). These findings strongly demonstrate that the developed ICG@PEG-CS/PDA NPS exhibit quite high PCE and robust colloidal photothermal stability, and reduce the photobleaching of ICG, thus being favorable to promote anticancer efficacy of ICG-mediated PTT and PDT.

3.4. Singlet oxygen generation and GSH depletion of ICG@PEG-CS/PDA NPS

Encouraged by the outstanding photothermal performance, the photo-activated singlet oxygen generation ability of ICG@PEG-CS/PDA NPS was explored by DPBF, a ROS indicator, that shows the decreased UV absorbance at about 410 nm in the presence of ROS. Under irradiation of 808 nm NIR laser, the absorbance of DPBF molecules in aqueous solutions containing ICG@PEG-CS/PDA NPS or free ICG molecules (ICG concentration = 65 μM) was appreciably decreased with the prolonged irradiation time (Fig. 5a and S8a), whereas the absorbance of DPBF molecules in aqueous solution of PEG-CS/PDA nanoparticles was virtually unchanged regardless of laser irradiation time (Fig. S8b). The results strongly verify that the ICG@PEG-CS/PDA NPS and free ICG molecules exposed to NIR irradiation could convert surrounding oxygen to singlet oxygen upon ICG-mediated photodynamic effect. Notably, with NIR laser irradiation time being increased, in comparison with free ICG molecules, the ICG@PEG-CS/PDA NPS led to appreciable decrease in the normalized absorbance of DPBF in solution (Fig. 5b). Furthermore, at the same laser irradiation time, the normalized ICG absorbances of ICG@PEG-CS/PDA NPS were remarkably higher than those of free ICG molecules (Fig. S9), illustrating again their superior photothermal stability. Based on these findings, it was concluded that the ICG@PEG-CS/PDA NPS moderately increased the ROS-generating ability of ICG molecules by reducing photo- and thermo-elicited degradation of ICG, thus showing promise in PDT application.

Despite the great potential of PDT in clinical cancer treatment, a high level of GSH in cancer cells can largely scavenge intracellular ROS to reduce oxidative injury, thus impacting the anticancer potency of PDT. To improve the PDT efficacy, it is essential to integrate the GSH-depleting material with PDT regents. Considering that PDA has been demonstrated to deplete GSH by Michael addition [39,56], the GSH consumption ability of ICG@PEG-CS/PDA NPS at 37 °C was assessed by DTNB assay. As presented in Fig. 5c and S10, with the reaction time of GSH treated with PEG-CS/PDA nanoparticles with or without ICG payloads being prolonged, the absorbance of the reduced DTNB at 412 nm in an aqueous solution containing the treated GSH molecules gradually decreased. Obviously, the quinone-rich PEG-CS/PDA nanoparticles could effectively consume GSH by irreversibly reacting with thiol groups of GSH upon Michael addition reaction. Note that, after 24 h reaction, the cumulative GSH depletion for ICG@PEG-CS/PDA NPS was somewhat lower than that for PEG-CS/PDA nanoparticles (Fig. 5d). It could be ascribed that ICG molecules attached on the surfaces of PEG-CS/PDA nanoparticles partially occupy reactive cites, thus hindering Michael addition of PDA with GSH. Importantly, in the presence of 100 μM GSH, taking advantage of the PDA-mediated GSH consumption, the ICG@PEG-CS/PDA NPS exposed to NIR irradiation still maintained satisfied ROS-generating capability as reflected by the appreciable decrease in normalized DTNB absorbance (Fig. 5b). By contrast, with laser irradiation, no significant reduction in the normalized absorbance of DTNB in aqueous solution containing free ICG and GSH was observed, indicating that the singlet oxygen generated by ICG-based photodynamic effect was largely scavenged by GSH. Furthermore, with the solution temperature being elevated from 37 to 50 °C, after 4-h reaction, the PEG-CS/PDA nanoparticles with or without ICG payloads displayed remarkably increased GSH depletion as compared to free ICG molecules (Fig. 5e), signifying that the Michael reaction between PDA and GSH could be accelerated by increasing reaction temperature. Such a thermo-enhanced PDA-mediated GSH consumption was also reported elsewhere

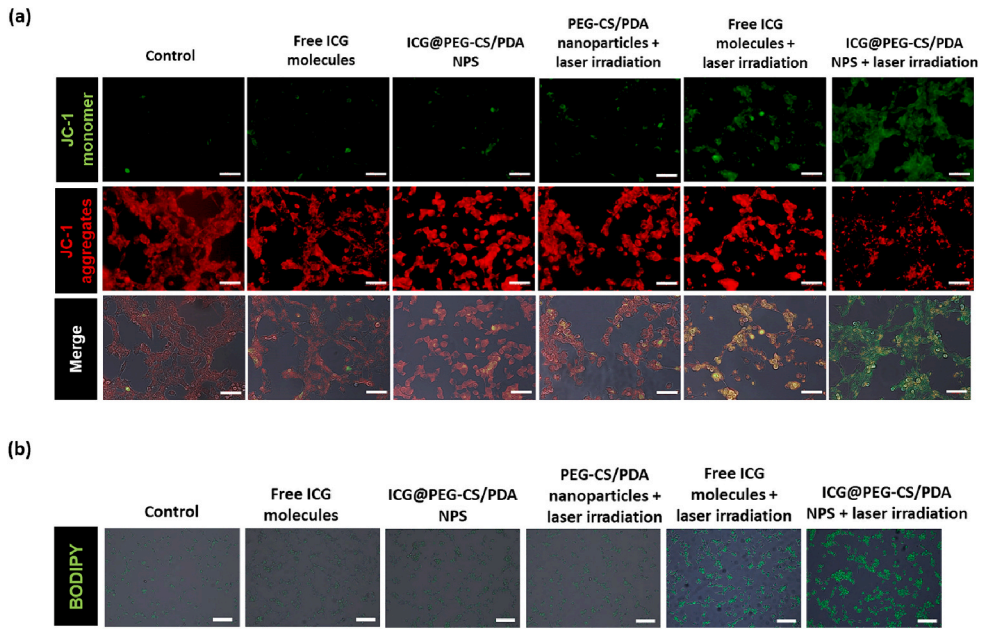

Fig. 7. (a) JC-1 and (b) BODIPY™ 581/591 C11 staining of CT26 cells receiving various treatments (JC-1 aggregates emit red fluorescence and JC-1 monomers emit green fluorescence). Scale bars are 50 μm.

[39,56]. In view of the above findings, it was anticipated that the ICG@PEG-CS/PDA NPS could largely boost anticancer potency of ICG-based PTT and PDT by photo-triggered hyperthermia and massive singlet oxygen generation with the aid of thermo-enhanced intracellular GSH consumption (Fig. 5f).

3.5. Cellular uptake, intracellular GSH depletion and singlet oxygen generation

The internalization of ICG@PEG-CS/PDA NPS by CT26 cells was studied by flow cytometry and CLSM. Free ICG molecules were used for comparison. Distinct from CT26 cells alone without fluorescence signals, CT26 cells incubated with ICG@PEG-CS/PDA NPS for 1 h showed appreciable ICG fluorescence signals, indicating the successful cellular uptake of these NPS via endocytosis (Fig. 6a). Moreover, with the incubation time being prolonged from 1 to 4 h, CT26 cells treated with ICG@PEG-CS/PDA NPS showed 2.9-fold increase in ICG fluorescence intensity. Also, the time-evolved increase in cellular uptake of ICG@PEG-CS/PDA NPS was confirmed by CLSM images (Fig. 6b). Similar findings were also attained for free ICG group (Fig. 6a and S11). Notably, in the absence of NIR laser irradiation, the intracellular GSH level of CT26 cells treated with PEG-CS/PDA nanoparticles was remarkably reduced from 80 % to 65 % with nanoparticle concentration being increased from 100 to 200 μg/mL (Fig. 6c). This suggests that the PEG-CS/PDA nanoparticles internalized by CT26 cells could moderately consume endogenous GSH via Michael addition. In a similar way, after being uptake by CT26 cells, the ICG@PEG-CS/PDA NPS also showed GSH-depleting capability (Fig. 6d). Especially, without laser irradiation, the intracellular GSH-consuming ability of ICG@PEG-CS/PDA NPS was slightly lower than that of PEG-CS/PDA NPS, being attributed to that ICG molecules attached on the surfaces of PEG-CS/PDA nanoparticles partially occupied reactive cites, thereby retarding interactions between PDA and GSH. Similar result was also observed in Fig. 5d. By contrast, no significant reduction in the intracellular GSH content of CT26 cells incubated with free ICG molecules was attained in the lack of laser irradiation, verifying the lack of GSH-consuming ability for ICG molecules. More importantly, with NIR irradiation, CT26 cells treated with ICG@PEG-CS/PDA NPS showed considerably declined intracellular GSH content compared to cells incubated with free ICG molecules or PEG-CS/PDA nanoparticles (Fig. 6d). A minor decrease in the intracellular GSH content of ICG-treated CT26 cells with laser irradiation could be attributed to that the singlet oxygen produced by ICG-mediated photodynamic effect somewhat consume GSH. In view of the higher PCE of ICG@PEG-CS/PDA NPS than that of PEG-CS/PDA nanoparticles (Fig. 4b and S6), it was concluded that the NIR-elicited powerful hyperthermia of ICG@PEG-CS/PDA NPS could speed up Michael reaction of intracellular GSH and PDA component, thus largely promoting GSH depletion, which being consistent with the results as presented in Fig. 5e. Also, undoubtedly, substantial singlet oxygen generated from the endocytosed ICG@PEG-CS/PDA NPS exposed to NIR irradiation contributed to intracellular GSH depletion.

The intracellular singlet oxygen generation of CT26 cells incubated with free ICG molecules and ICG@PEG-CS/PDA NPS, respectively, was measured by DCFH-DA probes using CLSM. In the lack of NIR irradiation, no significant DCF fluorescence in CT26 cells incubated with free ICG molecules or ICG@PEG-CS/PDA NPS was observed (Fig. 6e), indicating formation of few singlet oxygen. By contrast, with irradiation of 808 nm NIR laser, CT26 cells treated with free ICG molecules and ICG@PEG-CS/PDA NPS (ICG concentration = 5 μM), respectively, exhibited clearly visible DCF fluorescence, whereas CT26 cells incubated PEG-CS/PDA nanoparticles had no DCF fluorescence. This proves that the internalized free ICG molecules and ICG@PEG-CS/PDA NPS exposed to NIR laser irradiation could convert intracellular oxygen into singlet oxygen. More importantly, under NIR laser irradiation, the ICG@PEG-CS/PDA NPS group showed stronger DCF fluorescence than free ICG group, indicating that the former could effectively promote the accumulation of intracellular singlet oxygen by depleting endogenous GSH as described above.

3.6. Mitochondrial damage and LPO production

Several studies report that the mitochondria damage is a vital and characteristic hallmark of ROS-elicited apoptosis [12,42,57,58]. JC-1, a cationic fluorescent probe, is commonly utilized to identify the mitochondrial membrane potential. In healthy cells, JC-1 gathers in the mitochondrial matrix to create a polymer that emits red fluorescence. However, when the mitochondrial membrane potential decreases due to apoptosis, JC-1 transforms into a monomer that emits green

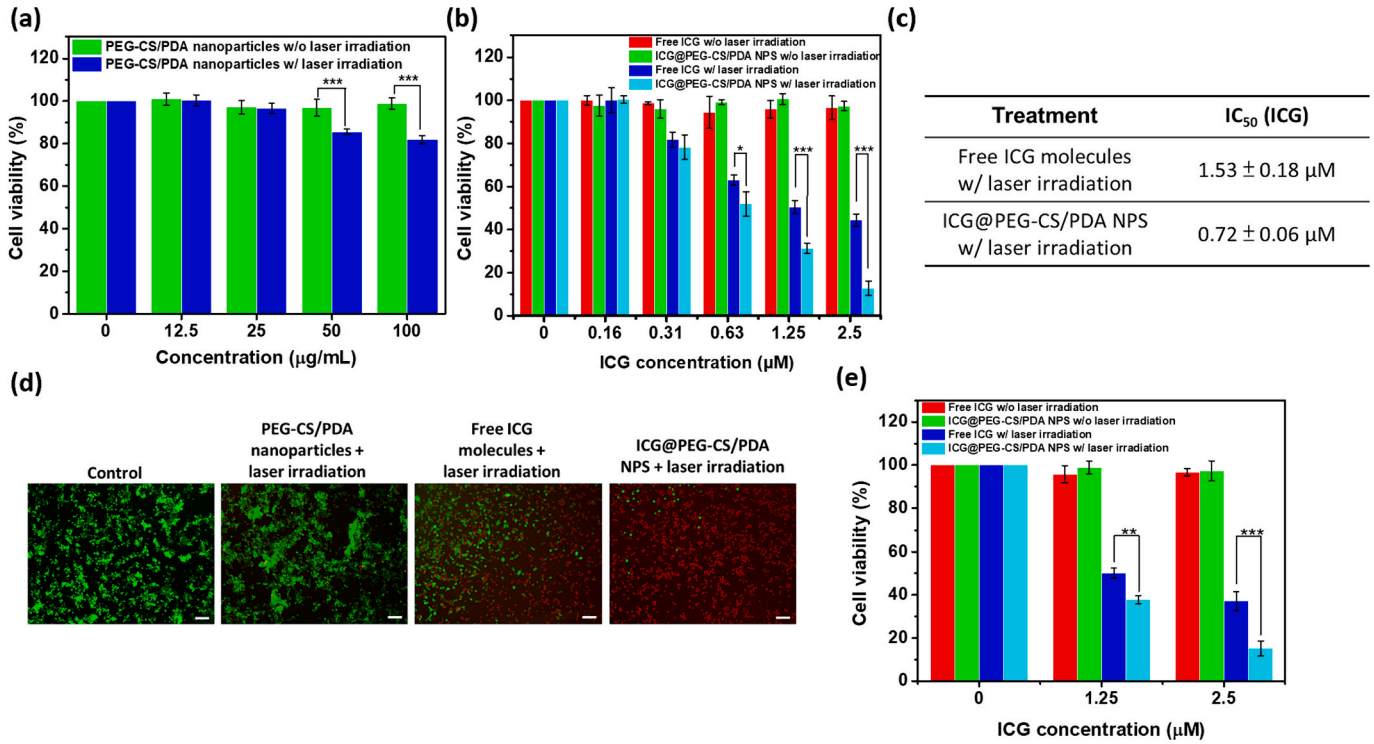

Fig. 8. Cell viability of CT26 cells treated with (a) PEG-CS/PDA nanoparticles and (b) various ICG-containing formulations, respectively, with or without 2-min NIR laser irradiation (1.0 W/cm^2), followed by additional 24 h incubation. (c) IC_{50} values of free ICG molecules and ICG@PEG-CS/PDA NPS exposed to laser irradiation on CT26 cells. (d) Fluorescence images of CT26 cells treated with free ICG molecules and PEG-CS/PDA nanoparticles with or without ICG payloads, respectively, plus 2-min NIR laser irradiation. The viable cells were stained green with calcein-AM and the dead cells were stained red with PI. Scale bars are 200 μm. (e) Cell viability of 4 T1 cells treated with various ICG-containing formulations with or without 2-min NIR laser irradiation (1.0 W/cm^2), followed by additional 24 h incubation. ns > 0.05, *p < 0.05, **p < 0.01, ***p < 0.001.

fluorescence. This colour alteration is a significant indication of the changes in the mitochondrial membrane potential [58–60]. As presented in Fig. 7a, in the lack of NIR laser irradiation, CT26 cells incubated with free ICG molecules or ICG@PEG-CS/PDA NPS only revealed red fluorescence comparable to the control group. In contrast, with NIR laser irradiation, the ICG@PEG-CS/PDA NPS treatment group exhibited stronger green fluorescence than free ICG group; while the PEG-CS/PDA nanoparticle group only showed weak green fluorescence. The above

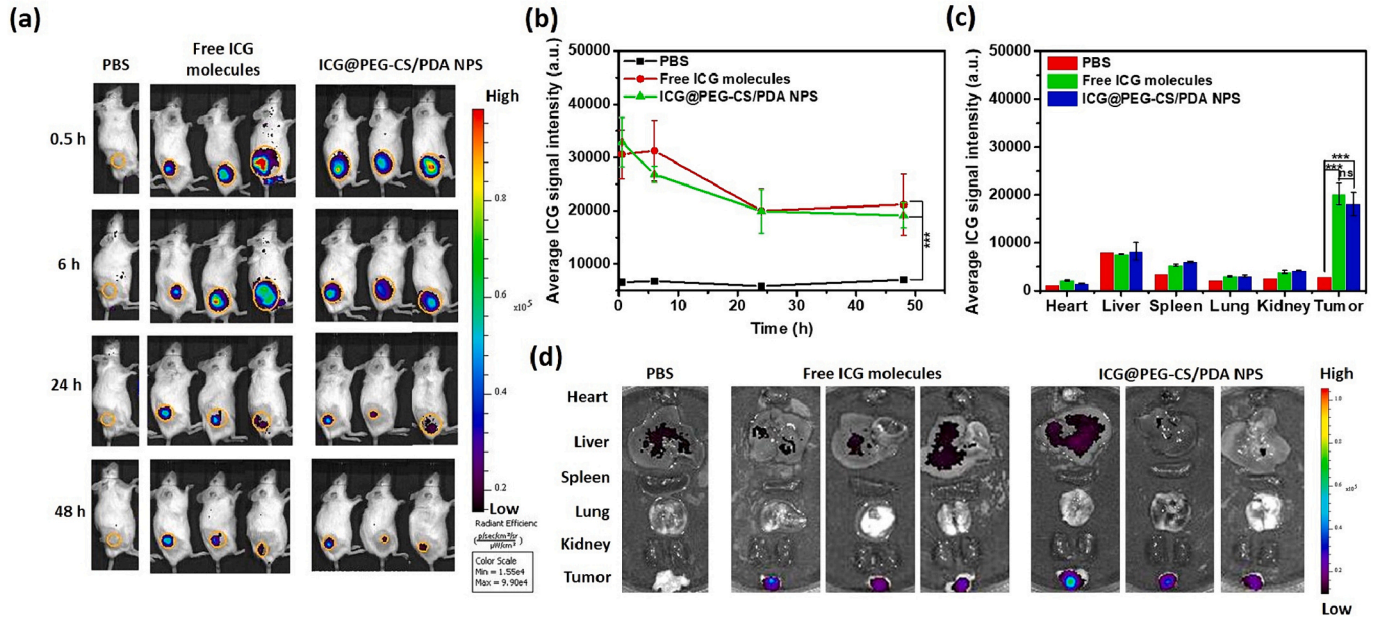

Fig. 9. (a) In vivo NIR fluorescence images and (b) ICG fluorescence signals of CT26 tumor-bearing mice receiving intratumoral injection of free ICG molecules or ICG@PEG-CS/PDA NPS by IVIS. The tumor sites were labeled with yellow circle. (c) Average ICG fluorescence intensities and (d) NIR fluorescence images of tumor and individual organs at 48 h post-intratumoral injection with free ICG molecules and ICG@PEG-CS/PDA NPS, respectively. ns > 0.05, *p < 0.05, **p < 0.01, ***p < 0.001.

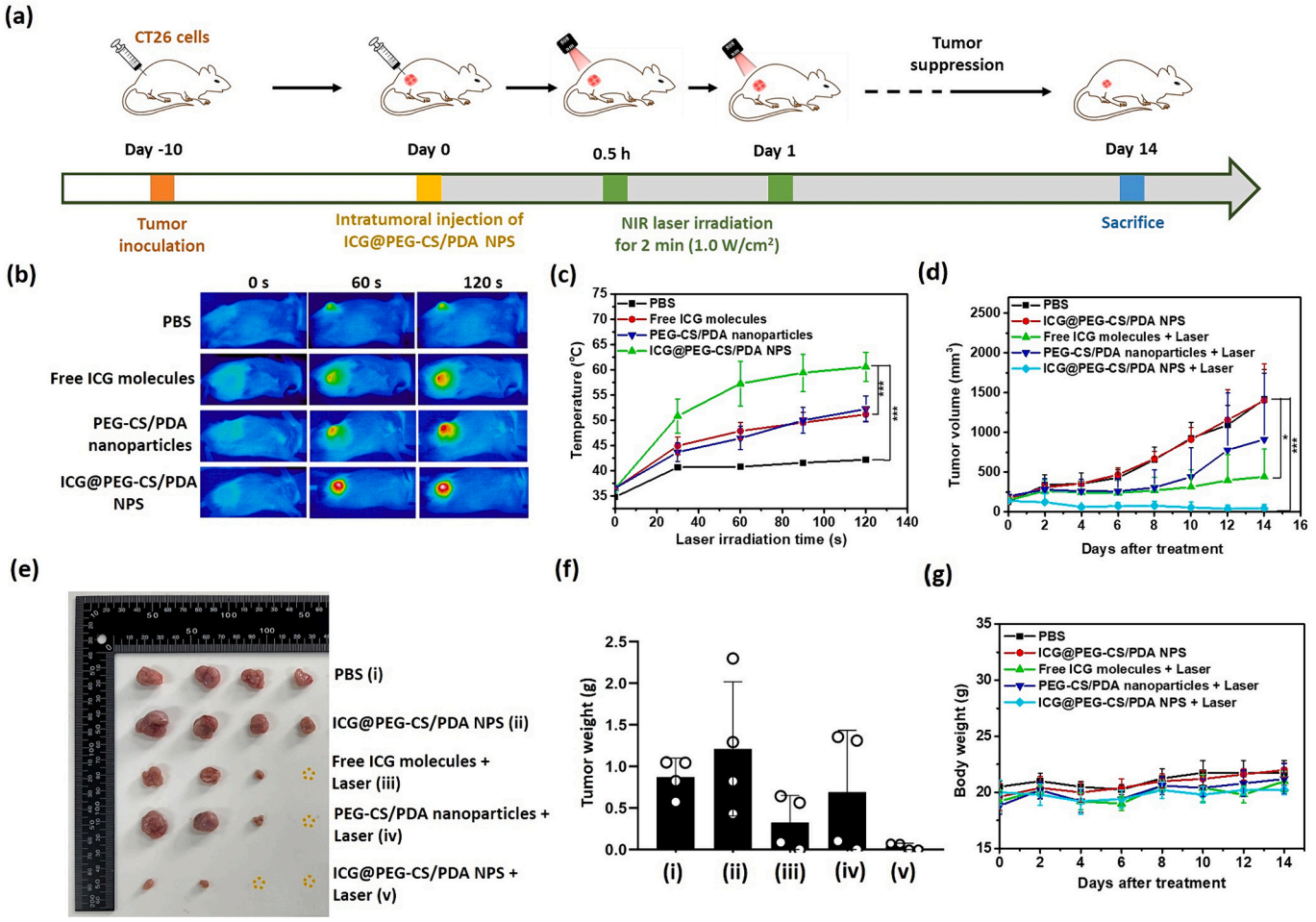

Fig. 10. (a) Schematic illumination of the in vivo treatment procedure on mice. (b) Infrared thermographic images and (c) temperature profiles of the tumor sites of CT26 tumor-bearing mice treated with PBS, free ICG molecules, PEG-CS/PDA nanoparticles or ICG@PEG-CS/PDA NPS and irradiated with 808 nm NIR laser (1.0 W/cm^2) for 2 min at 0.5 h post-intratumoral injection. (d) Tumor volume curves of CT26 tumor-bearing mice injected with various formulations, followed by followed by NIR laser irradiation (1.0 W/cm^2, 2 min) at 0.5 h and 24 h post-injection or without any laser irradiation. (e) Photographs and (f) weight of the tumors harvested from the euthanized mice at day 14 after the treatment. (g) Body weight of CT26 tumor-bearing mice receiving different treatments. ns > 0.05, *$p < 0.05$, **$p < 0.01$, ***$p < 0.001$.

findings demonstrate that the endocytosed ICG@PEG-CS/PDA NPS exposed to NIR irradiation could effectively product singlet oxygen with the aid of the PDA-mediated GSH depletion, thus potently destroying mitochondrial (Scheme 1b), whereas the internalized free ICG molecules under laser irradiation only showed limited mitochondrial damage due to the scavenging of singlet oxygen by endogenous GSH. On the other hand, considering that the intracellular singlet oxygen generation has been demonstrated to irreversibly oxidize the cellular unsaturated lipid into LPO, ultimately leading to ferroptosis, a type of iron-dependent non-apoptotic cell death [13,61,62], the formation of LPO induced by ICG@PEG-CS/PDA NPS was studied with BODIPY C11 as the probe. Notably, with NIR laser irradiation, CT26 cells incubated with ICG@PEG-CS/PDA NPS exhibited considerably stronger green fluorescence signals than cells treated with free ICG molecules or PEG-CS/PDA nanoparticles (Fig. 7b). In contrast, in the lack of NIR laser irradiation, no significant green fluorescence signals were observed in CT26 cells incubated with ICG-containing formulations. The results suggest that the ICG@PEG-CS/PDA NPS could prominently promote the intracellular accumulation of toxic LPO by NIR-triggered GSH consumption and singlet oxygen generation (Scheme 1b), while free ICG molecules only product limited LPO under laser irradiation owing to the consumption of ROS by intracellular GSH. Based on the above findings, it was expected that the ICG@PEG-CS/PDA NPS internalized by cancer cells could not only potently impair mitochondrial and generate LPO by NIR-elicited redox homeostasis imbalance but also ablate cancer cells upon NIR-triggered powerful hyperthermia, thus enhancing PDT/PTT-mediated anticancer effect.

3.7. *In vitro anticancer potency of the combined PTT and PDT*

To assess the anticancer effect of ICG-mediated PTT and PDT, the viability of CT26 cells incubated with either ICG@PEG-CS/PDA NPS or free ICG molecules with NIR laser irradiation was determined by MTT assay. As shown in Fig. 8a and b, in the lack of NIR irradiation, CT26 cells incubated with free ICG molecules or PEG-CS/PDA nanoparticles with or without ICG payloads maintained the high viability beyond 95 %, indicating that these formulations were non-toxic to cancer cells. Upon laser irradiation, the PEG-CS/PDA nanoparticles only showed slight anticancer activity against CT26 cells (ca 20 % cell death) despite the concentration of PEG-CS/PDA nanoparticles being increased to 100 μg/mL, signifying the limited therapeutic efficacy of PTT alone. Notably, the remarkable decrease in viability of CT26 cells treated with ICG@PEG-CS/PDA NPS or free ICG molecules (ICG concentration over 0.31 μM) was obtained with NIR laser irradiation, in particular for ICG@PEG-CS/PDA NPS. This illustrates that the ICG@PEG-CS/PDA NPS could effectively cause cancer cell death upon ICG-mediated PDT and PTT. Also, under NIR laser irradiation, the ICG dose required for 50 % cell cellular growth inhibition (IC_{50}) value of ICG@PEG-CS/PDA NPS

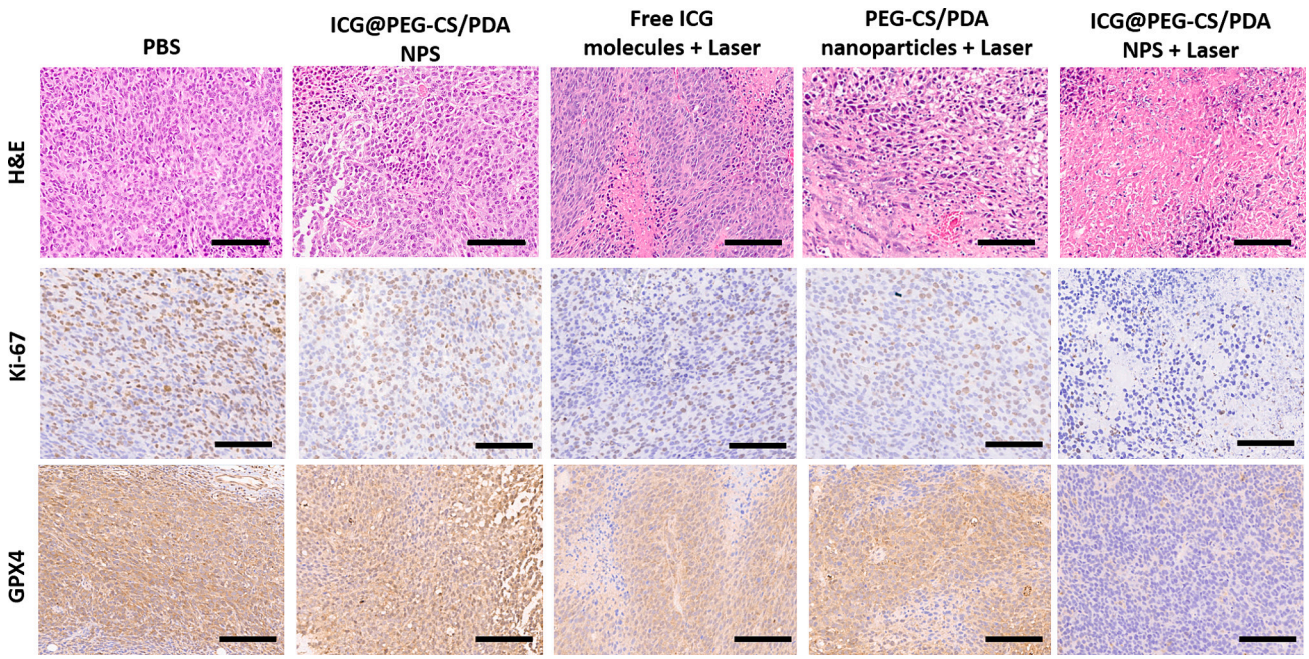

Fig. 11. H&E, Ki-67 and GPX4 staining of tumor slides from CT26 tumor-bearing mice receiving different treatments. Scale bars are 100 μm.

was attained to be ca 0.72 μM is 2.1-fold lower than that (1.53 μM) of free ICG molecules (Fig. 8c). At the same ICG concentration (1.25 μM) and 2-min NIR laser irradiation, most of CT26 cells treated with ICG@PEG-CS/PDA NPS exhibited significant PI-positive staining relative to cells receiving free ICG molecules (Fig. 8d). The same findings were attained with another cell model, 4 T1 cancer cells (Fig. 8e and S12). Such a prominent NIR-triggered anticancer efficacy of ICG@PEG-CS/PDA NPS superior to free ICG molecules could be attributed to the following reasons. First, compared to free ICG molecules, the ICG@PEG-CS/PDA NPS under laser irradiation showed higher photothermal effect and better ROS-generating ability by reducing ICG photobleaching as revealed in Fig. 4a and 5b. Additionally, the ICG@PEG-CS/PDA NPS efficiently consumed intracellular GSH to promote accumulation of singlet oxygen within cancer cells, thereby leading to remarkable mitochondrial damage and LPO generation (Scheme 1b).

3.8. In vivo biodistribution

As presented in several studies [63,64], after being administered intravenously, free ICG molecules showed quite lower tumor accumulation than ICG-carrying nanoparticles due to their poor aqueous stability and quick body clearance. To objectively evaluate the difference in the antitumor efficacy between free ICG molecules and ICG@PEG-CS/PDA NPS based on ICG-mediated phototherapy, it is essential to ensure the equal intratumoral ICG accumulation of free ICG molecules and ICG@PEG-CS/PDA NPS. To this end, free ICG molecules and ICG@PEG-CS/PDA NPS were intratumorally injected, respectively, into CT26 tumor-bearing mice at a dosage of 0.1 mg/kg ICG. As revealed in Fig. 9a and b, the tumor sites injected with free ICG molecules and ICG@PEG-CS/PDA NPS, respectively, exhibited similar ICG fluorescence intensity from 0.5 to 48 h post injection. Also, the ex vivo ICG fluorescence signals of tumors receiving free ICG molecules was comparable to those of tumors treated with ICG@PEG-CS/PDA NPS (Fig. 9c and d). Undoubtedly, through the intratumoral injection of free ICG molecules and ICG@PEG-CS/PDA NPS, the equal amount of ICG accumulation within tumor was realized. On the other hand, for free ICG and ICG@PEG-CS/PDA NPS groups, the tumor sites showed strongest ex vivo ICG fluorescence intensity than other organs, corresponding to the typical biodistribution of ICG molecules injected intratumorally.

3.9. In vivo antitumor potency of the combined PTT and PDT

Encouraged by the brilliant in vitro anticancer performance, the in vivo photo-triggered antitumor efficacy of ICG@PEG-CS/PDA NPS on CT26 tumor-bearing mice was further explored (Fig. 10a). First, to confirm the NIR-triggered hyperthermia capability of ICG@PEG-CS/PDA NPS on the tumor, the temperature change of tumor receiving PBS as the control, free ICG molecules, PEG-CS/PDA nanoparticles and ICG@PEG-CS/PDA NPS, respectively, exposed to irradiation of 808 nm laser, was monitored by the infrared thermal imaging camera. As shown in Fig. 10b and c, compared to PBS group with few temperature elevation of tumor, other three groups displayed appreciably increased tumor temperature (beyond 50 °C), in particular for ICG@PEG-CS/PDA NPS. The NIR-activated hyperthermia of ICG@PEG-CS/PDA NPS superior to free ICG molecules could be attributed to that the former exhibit higher PCE and lower ICG photobleaching degree than the latter (Fig. 4b, e, S6, S7 and S9). However, the temperature of tumor in the ICG@PEG-CS/PDA NPS group eventually exceeded 60 °C within 2 min, thus inevitably causing inflammation and collateral damage to the surrounding healthy tissues. Some studies reported that mild PTT, whose temperature range is usually controlled from 42 to 45 °C, could reduce the side effects of PTT [65,66]. Considering that the ICG@PEG-CS/PDA NPS exhibited a photothermal effect that varied with concentration and laser irradiation time (Fig. 4c and 10c), it is essential to optimize the dose of ICG@PEG-CS/PDA NPS as well as laser irradiation time during treatment to ensure the biosafety. We also observed the mice in different treatment groups for 14 days post intratumoral injection and recorded the variations of tumor volume and body weight to investigate the antitumor effects of combined PTT and PDT. In the absence of NIR laser irradiation, a remarkable enlargement in the tumor volume of mice treated with ICG@PEG-CS/PDA NPS similar to that of PBS group was observed (Fig. 10d and S13), suggesting the failure of tumor growth suppression owing to the lack of PTT and PDT. Notably, with 2-min NIR laser irradiation, the administration of ICG@PEG-CS/PDA NPS effectively inhibited tumor growth in comparison with that of free ICG molecules and PEG-CS/PDA nanoparticles during treatment process. In agreement with the data of in vivo tumor growth inhibition, in addition to complete disappearance of some tumors, the size and weight of tumors collected from the mice treated with ICG@PEG-CS/PDA NPS plus

laser irradiation were the smallest among the tumor receiving other treatments (Fig. 10e and f). The above findings demonstrate that the ICG@PEG-CS/PDA NPS could substantially boost the antitumor potency of ICG-mediated PTT and PDT by NIR-elicited powerful hyperthermia and redox homeostasis disturbance. By contrast, free ICG molecules and PEG-CS/PDA nanoparticles exposed to laser irradiation only displayed limited antitumor effect. For free ICG molecules, the NIR-triggered singlet oxygen production and hyperthermia within tumor sites were largely impacted by the endogenous GSH and severe ICG photobleaching. Moreover, the inadequate and nonuniform photothermal effect of PEG-CS/PDA nanoparticles within tumor region restricted their PTT-based antitumor efficacy. On the other hand, the treated mice in all groups showed nearly unchanged body weight (Fig. 10g), indicating that these formulations did not lead to acute side effect.

In the H&E staining images of the tumor sections (Fig. 11), the ICG@PEG-CS/PDA NPS plus laser group showed more nuclear fragmentation and lower cell density as compared to other groups. Similarly, a remarkable decline in Ki67 proliferation staining was observed in the tumor sections of ICG@PEG-CS/PDA NPS plus laser group. These results illustrate that the combined phototherapy delivered by ICG@PEG-CS/PDA NPS could display strong anti-proliferative effects. Furthermore, as presented in GPX4-stained images, the tumor sections of ICG@PEG-CS/PDA NPS-treated mice with NIR laser irradiation showed significantly decreased expression of GPX4 in comparison with those of other treatment groups. This could be ascribed to that the ICG@PEG-CS/PDA NPS exposed to NIR irradiation can largely deplete GSH of tumor cells by singlet oxygen and PDA-mediated Michael reaction, thus leading to GPX4 inactivation. Some previous studies reported that the inhibited activity of GPX4 in cancer cells appreciably decreased ability of tumor to scavenge free radicals, thereby resulting in LPO accumulation to induce ferroptosis [42,59,67,68]. On the other hand, no appreciable abnormality was observed in major organs of mice receiving ICG-containing formulations with laser irradiation (Fig. S14), because the NIR irradiation as hyperthermia and ROS trigger was utilized exclusively on tumors only. Based on the above findings, it can be concluded that the reinforced dual-modal phototherapy delivered by ICG@PEG-CS/PDA NPS developed in this work could achieve NIR-triggered potent redox homeostasis disruption and hyperthermia to promote intracellular mitochondrial damage and LPO accumulation, thus effectively suppressing tumor growth without significant systemic toxicity (Scheme 1b).

4. Conclusions

To maximize antitumor potency of the combined PTT and PDT, the PEG-CS conjugate was synthesized and then decorated on the surfaces of PDA nanoparticles for ICG delivery. Through the multiple interactions between ICG molecules and PEG-CS/PDA nanoparticles, the resulting ICG@PEG-CS/PDA NPS not only exhibited sound ICG loading capacity and prominent PCE (62.8 %) but also remarkably promoted photothermal stability and singlet oxygen-generating ability of ICG molecules. Moreover, these NPS realized sustained ICG release. After being internalized by CT26 cancer cells, the NPS under NIR laser irradiation effectively produced hyperthermia and massive singlet oxygen with the assistance of PDA-mediated GSH depletion, thereby promoting mitochondrial damage and LPO generation to induce cell apoptosis and ferroptosis. More importantly, in comparison with free ICG molecules and PEG-CS/PDA nanoparticles, the ICG@PEG-CS/PDA NPS generated powerful hyperthermia on tumor in vivo by NIR laser irradiation. By the enhanced PTT combined with self-augmented PDT, the NPS prominently suppressed tumor growth without systemic adverse effect. Over all, the ICG@PEG-CS/PDA NPS featured with prominent GSH-depleting, singlet oxygen-generating and photothermal conversion capabilities as well as sound photothermal stability show great potential in tumor treatment of the combined PTT and PDT.

CRediT authorship contribution statement

Yu-Hsin Chen: Project administration, Methodology, Investigation, Formal analysis, Data curation. **I-Ju Liu:** Visualization, Validation, Methodology, Formal analysis. **Tzu-Chen Lin:** Validation, Methodology, Investigation, Formal analysis. **Min-Chen Tsai:** Validation, Methodology, Data curation. **Shang-Hsiu Hu:** Resources, Methodology, Investigation. **Tsai-Ching Hsu:** Supervision, Resources, Investigation. **Yi-Ting Wu:** Visualization, Resources, Methodology, Formal analysis. **Bor-Show Tzang:** Writing – original draft, Supervision, Resources, Investigation, Funding acquisition. **Wen-Hsuan Chiang:** Writing – review & editing, Writing – original draft, Supervision, Resources, Investigation, Funding acquisition, Conceptualization.

Declaration of competing interest

The authors declare that they have no known competing financial interests or personal relationships that could have appeared to influence the work reported in this paper.

Data availability

Data will be made available on request.

Acknowledgements

This work is supported by the National Science and Technology Council (MOST 111-2628-E-005-009-MY2), National Chung Hsing University and Chung Shan Medical University (NCHU-CSMU 11202), Taiwan.

Appendix A. Supplementary data

Supplementary data to this article can be found online at https://doi.org/10.1016/j.ijbiomac.2024.131359.

References

[1] Q. Guan, L.L. Zhou, Y.A. Li, W.Y. Li, S. Wang, C. Song, Y.B. Dong, Nanoscale covalent organic framework for combinatorial antitumor photodynamic and photothermal therapy, ACS Nano 13 (2019) 13304–13316.
[2] X. Wang, Z. Li, Y. Ding, K. Wang, Z. Xing, X. Sun, W. Guo, X. Hong, X. Zhu, Y. Liu, Enhanced photothermal-photodynamic therapy for glioma based on near-infrared dye functionalized Fe_3O_4 superparticles, Chem. Eng. J. 381 (2020) 122693.
[3] L. Feng, R. Zhao, L. Yang, B. Liu, S. Dong, C. Qian, J. Liu, Y. Zhao, Tumor-specific NIR-activatable nanoreactor for self-enhanced multimodal imaging and cancer phototherapy, ACS Nano 17 (2023) 1622–1637.
[4] C.C. Hung, W.C. Huang, Y.W. Lin, T.W. Yu, H.H. Chen, S.C. Lin, W.H. Chiang, H. C. Chiu, Active tumor permeation and uptake of surface charge-switchable theranostic nanoparticles for imaging-guided photothermal/chemo combinatorial therapy, Theranostics 6 (2016) 302–317.
[5] X. Deng, Z. Shao, Y. Zhao, Solutions to the drawbacks of photothermal and photodynamic cancer therapy, Adv. Sci. 8 (2021) 2002504.
[6] X. Li, J.F. Lovell, J. Yoon, X. Chen, Clinical development and potential of photothermal and photodynamic therapies for cancer, Nat. Rev. Clin. Oncol. 17 (2020) 657–674.
[7] Z. Xie, T. Fan, J. An, W. Choi, Y. Duo, Y. Ge, B. Zhang, G. Nie, N. Xie, T. Zheng, Y. Chen, H. Zhang, J.S. Kim, Emerging combination strategies with phototherapy in cancer nanomedicine, Chem. Soc. Rev. 49 (2020) 8065–8087.
[8] Q. Xu, Y. Yang, J. Lu, Y. Lin, S. Feng, X. Luo, D. Di, S. Wang, Q. Zhao, Recent trends of mesoporous silica-based nanoplatforms for nanodynamic therapies, Coord. Chem. Rev. 469 (2022) 214687.
[9] H. Xu, Y. Zhang, H. Zhang, Y. Zhang, Q. Xu, J. Lu, S. Feng, X. Luo, S. Wang, Q. Zhao, Smart polydopamine-based nanoplatforms for biomedical applications: state-of-art and further perspectives, Coord. Chem. Rev. 488 (2023) 215153.
[10] S. Feng, J. Wang, X. Mu, G. Gu, Y. Wang, J. Lu, S. Wang, Q. Zhao, Mesoporous carbon nanoenzyme as nano-booster for photothermal-enhanced photodynamic therapy compared with graphene oxide, Colloids Surf. B: Biointerfaces 222 (2023) 113095.
[11] F. Liu, S. Gong, M. Shen, T. He, X. Liang, Y. Shu, X. Wang, S. Ma, X. Li, M. Zhang, Q. Wu, C. Gong, A glutathione-activatable nanoplatform for enhanced photodynamic therapy with simultaneous hypoxia relief and glutathione depletion, Chem. Eng. J. 403 (2021) 126305.

[12] S. Xiao, Y. Lu, M. Feng, M. Dong, Z. Cao, X. Zhang, Y. Chen, J. Liu, Multifunctional FeS_2 theranostic nanoparticles for photothermal-enhanced chemodynamic/photodynamic cancer therapy and photoacoustic imaging, Chem. Eng. J. 396 (2020) 125294.
[13] H. Cheng, Y. He, J. Lu, Z. Yan, L. Song, Y. Mao, D. Di, Y. Gao, Q. Zhao, S. Wang, Degradable iron-rich mesoporous dopamine as a dual-glutathione depletion nanoplatform for photothermal-enhanced ferroptosis and chemodynamic therapy, J. Colloid Interface Sci. 639 (2023) 249–262.
[14] N. Kwon, G.O. Jasinevicius, G. Kassab, L. Ding, J. Bu, L.P. Martinelli, V.G. Ferreira, A. Dhaliwal, H.H.L. Chan, Y. Mo, V.S. Bagnato, C. Kurachi, J. Chen, G. Zheng, H. H. Buzzá, Nanostructure-driven indocyanine green dimerization generates ultra-stable phototheranostics nanoparticles, Angew. Chem. Int. Ed. 62 (2023) e202305564.
[15] W. Miao, H. Kim, V. Gujrati, J.Y. Kim, H. Jon, Y. Lee, M. Choi, J. Kim, S. Lee, D. Y. Lee, S. Kang, S. Jon, Photo-decomposable organic nanoparticles for combined tumor optical imaging and multiple phototherapies, Theranostics 6 (2016) 2367.
[16] R. Kv, T.I. Liu, I.L. Lu, C.C. Liu, H.H. Chen, T.Y. Lu, W.H. Chiang, H.C. Chiu, Tumor microenvironment-responsive and oxygen self-sufficient oil droplet nanoparticles for enhanced photothermal/photodynamic combination therapy against hypoxic tumors, J. Control. Release 328 (2020) 87–99.
[17] Y. Dai, J. Su, K. Wu, W. Ma, B. Wang, M. Li, P. Sun, Q. Shen, Q. Wang, Q. Fan, Multifunctional thermosensitive liposomes based on natural phase-change material: near-infrared light-triggered drug release and multimodal imaging-guided cancer combination therapy, ACS Appl. Mater. Interfaces 11 (2019) 10540–10553.
[18] B. Ryplida, G. Lee, I. In, S.Y. Park, Zwitterionic carbon dot-encapsulating pH-responsive mesoporous silica nanoparticles for NIR light-triggered photothermal therapy through pH-controllable release, Biomater. Sci. 7 (2019) 2600–2610.
[19] G. Yeroslavsky, M. Umezawa, K. Okubo, K. Nigoghossian, D.T.K. Dung, K. Miyata, M. Kamimura, K. Soga, Stabilization of indocyanine green dye in polymeric micelles for NIR-II fluorescence imaging and cancer treatment, Biomater. Sci. 8 (2020) 2245–2254.
[20] Z. Dong, H. Gong, M. Gao, W. Zhu, X. Sun, L. Feng, T. Fu, Y. Li, Z. Liu, Polydopamine nanoparticles as a versatile molecular loading platform to enable imaging-guided cancer combination therapy, Theranostics 6 (2016) 1031–1042.
[21] X.L. Xu, M.X. Chen, X.F. Lou, Y.Y. Du, G.F. Shu, J. Qi, M.L. Zhu, X.Y. Ying, L. Yu, J. S. Ji, Y.Z. Du, Sialic acid-modified mesoporous polydopamine induces tumor vessel normalization to enhance photodynamic therapy by inhibiting VE-cadherin internalization, Chem. Eng. J. 414 (2021) 128743.
[22] T. Yan, G. Alimu, L. Zhu, H. Fan, L. Zhang, Z. Du, R. Ma, S. Chen, N. Alifu, X. Zhang, PpIX/IR-820 dual-modal therapeutic agents for enhanced PDT/PTT synergistic therapy in cervical cancer, ACS Omega 7 (2022) 44643–44656.
[23] F. Guo, M. Yu, J. Wang, F. Tan, N. Li, The mitochondria-targeted and IR780-regulated theranosomes for imaging and enhanced photodynamic/photothermal therapy, RSC Adv. 6 (2016) 11070–11076.
[24] Q. Dai, E. Ren, D. Xu, Y. Zeng, C. Chen, G. Liu, Indocyanine green-based nanodrugs: a portfolio strategy for precision medicine, Prog, Nat. Sci. Mater. 30 (2020) 577–588.
[25] W. Lu, W. Liu, A. Hu, J. Shen, H. Yi, Z. Cheng, Combinatorial polydopamine-liposome nanoformulation as an effective anti-breast cancer therapy, Int. J. Nanomedicine 18 (2023) 861–879.
[26] H. Cao, Y. Yang, M. Liang, Y. Ma, N. Sun, X. Gao, J. Li, Pt@polydopamine nanoparticles as nanozymes for enhanced photodynamic and photothermal therapy, Chem. Commun. 57 (2021) 255–258.
[27] L. Yang, C. Zhang, J. Liu, F. Huang, Y. Zhang, X.J. Liang, J. Liu, ICG-conjugated and 125 I-labeled polymeric micelles with high biosafety for multimodality imaging-guided photothermal therapy of tumors, Adv. Healthc. Mater. 9 (2020) e1901616.
[28] L. Yang, B. Huang, S. Hu, Y. An, J. Sheng, Y. Li, Y. Wang, N. Gu, Indocyanine green assembled free oxygen-nanobubbles towards enhanced near-infrared induced photodynamic therapy, Nano Res. 15 (2022) 4285–4293.
[29] F. Gao, L. Jiang, J. Zhang, Y. Chang, W. Gao, L. Ding, G. Ma, X. Ma, Y. Guo, Near-infrared light-responsive nanosystem with prolonged circulation and enhanced penetration for increased photothermal and photodynamic therapy, ACS Materials Lett. 5 (2022) 1–10.
[30] K. Gowsalya, V. Yasothamani, R. Vivek, Emerging indocyanine green-integrated nanocarriers for multimodal cancer therapy: a review, Nanoscale Adv. 3 (2021) 3332–3352.
[31] M.H. Hsieh, T.H. Wang, S.H. Hu, T.C. Hsu, J.L. Yow, B.S. Tzang, W.H. Chiang, Tumor site-specific PEG detachment and active tumor homing of therapeutic PEGylated chitosan/folate-decorated polydopamine nanoparticles to augment antitumor efficacy of photothermal/chemo combination therapy, Chem. Eng. J. 446 (2022) 137243.
[32] S. Liu, J. Pan, J. Liu, Y. Ma, F. Qiu, L. Mei, X. Zeng, G. Pan, Dynamically PEGylated and borate-coordination-polymer-coated polydopamine nanoparticles for synergetic tumor-targeted, chemo-photothermal combination therapy, Small 14 (2018) 1703968.
[33] J. Lu, L. Song, S. Feng, K. Wang, Y. Mao, Y. Gao, Q. Zhao, S. Wang, Nanozyme-mediated biocatalysis as a mitochondrial oxidative stress amplifier for tumor nanocatalytic immunotherapy, Chem. Eng. J. 481 (2024) 148270.
[34] W. Zeng, Z. Li, Q. Huang, C. Ding, L. Yang, W. Wang, Z. Shi, Y. Yang, H. Chen, L. Mei, X. Zeng, Multifunctional mesoporous polydopamine-based systematic delivery of STING agonist for enhanced synergistic photothermal-immunotherapy, Adv. Funct. Mater. 34 (2024) 2307241.
[35] P. Sun, Z. Li, D. Zhang, W. Zeng, Y. Zheng, L. Mei, H. Chen, N. Gao, X. Zeng, Multifunctional biodegradable nanoplatform based on oxaliplatin prodrug cross-linked mesoporous polydopamine for enhancing cancer synergetic therapy, Chin. Chem. Lett. 35 (2024) 108346.
[36] P. Huang, Y. Yang, W. Wang, Z. Li, N. Gao, H. Chen, X. Zeng, Self-driven nanoprodrug platform with enhanced ferroptosis for synergistic photothermal-IDO immunotherapy, Biomaterials 299 (2023) 122157.
[37] L. Yang, D. Zhang, W. Li, H. Lin, C. Ding, Q. Liu, L. Wang, Z. Li, L. Mei, H. Chen, Y. Zhao, X. Zeng, Biofilm microenvironment triggered self-enhancing photodynamic immunomodulatory microneedle for diabetic wound therapy, Nat. Commun. 14 (2023) 7658.
[38] L. Chen, Z. Lin, L. Liu, X. Zhang, W. Shi, D. Ge, Y. Sun, Fe^{2+}/Fe^{3+} ions chelated with ultrasmall polydopamine nanoparticles induce ferroptosis for cancer therapy, ACS Biomater Sci. Eng. 5 (2019) 4861–4869.
[39] J. Xiao, L. Hai, Y. Li, H. Li, M. Gong, Z. Wang, Z. Tang, L. Deng, D. He, An ultrasmall Fe_3O_4-decorated polydopamine hybrid nanozyme enables continuous conversion of oxygen into toxic hydroxyl radical via GSH-depleted cascade redox reactions for intensive wound disinfection, Small 18 (2022) 2105465.
[40] H. Hu, X. Liu, J. Hong, N. Ye, C. Xiao, J. Wang, Z. Li, D. Xu, Mesoporous polydopamine-based multifunctional nanoparticles for enhanced cancer phototherapy, J. Colloid Interface Sci. 612 (2022) 246–260.
[41] L. Zhang, Y. Fan, Z. Yang, M. Yang, C.Y. Wong, NIR-II-driven and glutathione depletion-enhanced hypoxia-irrelevant free radical nanogenerator for combined cancer therapy, J. Nanobiotechnology 19 (2021) 265.
[42] Z. Zhang, D. Ding, J. Liu, C. Huang, W. Li, K. Lu, N. Cheng, Supramolecular nanozyme system based on polydopamine and polyoxometalate for photothermal-enhanced multienzyme cascade catalytic tumor therapy, ACS Appl. Mater. Interfaces 15 (2023) 38214–38229.
[43] Z. Du, R. Ma, S. Chen, H. Fan, Y. Heng, T. Yan, G. Alimu, L. Zhu, X. Zhang, N. Alifu, C. Ma, A highly efficient polydopamine encapsulated clinical ICG theranostic nanoplatform for enhanced photothermal therapy of cervical cancer, Nanoscale Adv. 4 (2022) 4016–4024.
[44] X. Liu, N. Xu, X. Pu, J. Wang, X. Liao, Z. Huang, G. Yin, Combined photothermal-photodynamic therapy by indocyanine green loaded polydopamine nanoparticles enhances anti-mammary gland tumor efficacy, J. Mater. Chem. B 10 (2022) 4605–4614.
[45] H.J. Huang, S.Y. Huang, T.H. Wang, T.Y. Lin, N.C. Huang, O. Shih, U.S. Jeng, C. Y. Chu, W.H. Chiang, Clay nanosheets simultaneously intercalated and stabilized by PEGylated chitosan as drug delivery vehicles for cancer chemotherapy, Carbohydr. Polym. 302 (2023) 120390.
[46] S.Y. Huang, N.T. Yeh, T.H. Wang, T.C. Hsu, H.Y. Chin, B.S. Tzang, W.H. Chiang, Onion-like doxorubicin-carrying polymeric nanomicelles with tumor acidity-sensitive dePEGylation to expose positively-charged chitosan shell for enhanced cancer chemotherapy, Int. J. Biol. Macromol. 227 (2023) 925–937.
[47] Y.L. Liu, T.H. Wang, N.T. Yeh, W.J. Huang, B.S. Tzang, I.T. Wu, H.Y. Chin, S.H. Hu, T.C. Hsu, W.H. Chiang, Tumor-activated targetable photothermal chemotherapy using IR780/zoledronic acid-containing hybrid polymeric nanoassemblies with folate modification to treat aggressive breast cancer, Nanoscale 16 (2024) 1415–1427.
[48] R. Chen, C. Zhu, Y. Fan, W. Feng, J. Wang, E. Shang, Q. Zhou, Z. Chen, Polydopamine-based multifunctional platform for combined photothermal therapy, chemotherapy, and immunotherapy in malignant tumor treatment, ACS Appl. Bio Mater. 2 (2019) 874–883.
[49] D. Sprouse, Y. Jiang, J.E. Laaser, T.P. Lodge, T.M. Reineke, Tuning cationic block copolymer micelle size by pH and ionic strength, Biomacromolecules 17 (2016) 2849–2859.
[50] V.T.A. Nguyen, M.C. De Pauw-Gillet, O. Sandre, M. Gauthier, Biocompatible polyion complex micelles synthesized from arborescent polymers, Langmuir 32 (2016) 13482–13492.
[51] A. Vincy, N. Bhatia, R. Vankayala, Optical characteristics of indocyanine green J-aggregates induced by cisplatin for phototheranostic applications, ACS Biomater Sci. Eng. 8 (2022) 5119–5128.
[52] S. Wang, G. Hüttmann, F. Rudnitzki, H. Diddens-Tschoeke, Z. Zhang, R. Rahmanzadeh, Indocyanine green as effective antibody conjugate for intracellular molecular targeted photodynamic therapy, J. Biomed. Opt. 21 (2016) 078001.
[53] Y. Li, G. Liu, J. Ma, J. Lin, H. Lin, G. Su, D. Chen, S. Ye, X. Chen, X. Zhu, Z. Hou, Chemotherapeutic drug-photothermal agent co-self-assembling nanoparticles for near-infrared fluorescence and photoacoustic dual-modal imaging-guided chemo-photothermal synergistic therapy, J. Control. Release 258 (2017) 95–107.
[54] X. Li, T. Yong, Z. Wei, N. Bie, X. Zhang, G. Zhan, J. Li, J. Qin, J. Yu, B. Zhang, L. Gan, X. Yang, Reversing insufficient photothermal therapy-induced tumor relapse and metastasis by regulating cancer-associated fibroblasts, Nat. Commun. 13 (2022) 2794.
[55] J. Zhang, K. Zhang, Y. Hao, H. Yang, J. Wang, Y. Zhang, W. Zhao, S. Ma, C. Mao, Polydopamine nanomotors loaded indocyanine green and ferric ion for photothermal and photodynamic synergistic therapy of tumor, J. Colloid Interface Sci. 633 (2023) 679–690.
[56] T.H. Wang, M.Y. Shen, N.T. Yeh, Y.H. Chen, T.C. Hsu, H.Y. Chin, Y.T. Wu, B. S. Tzang, W.H. Chiang, Photothermal nanozymes to self-augment combination cancer therapy by dual-glutathione depletion and hyperthermia/acidity-activated hydroxyl radical generation, J. Colloid Interface Sci. 650 (2023) 1698–1714.
[57] J. Morgan, A.R. Oseroff, Mitochondria-based photodynamic anti-cancer therapy, Adv. Drug Deliv. Rev. 49 (2001) 71–86.
[58] J. Zhuang, B. Wang, H. Chen, K. Zhang, N. Li, N. Zhao, B.Z. Tang, Efficient NIR-II type-I AIE photosensitizer for mitochondria-targeted photodynamic therapy through synergistic apoptosis-ferroptosis, ACS Nano 17 (2023) 9110–9125.

[59] Z. Liu, S. Liu, B. Liu, Y. Bian, M. Yuan, C. Yang, Q. Ming, C. Chen, P. Ma, J. Lin, Fe (III)-naphthazarin metal-phenolic networks for glutathione-depleting enhanced ferroptosis-apoptosis combined cancer therapy, Small 19 (2023) 2207825.
[60] W. Xu, T. Wang, J. Qian, J. Wang, G. Hou, Y. Wang, X. Cui, A. Suo, D. Wu, Fe (II)-hydrazide coordinated all-active metal organic framework for photothermally enhanced tumor penetration and ferroptosis-apoptosis synergistic therapy, Chem. Eng. J. 437 (2022) 135311.
[61] L. Ke, F. Wei, L. Xie, J. Karges, Y. Chen, L. Ji, H. Chao, A biodegradable iridium (III) coordination polymer for enhanced two-photon photodynamic therapy using an apoptosis-ferroptosis hybrid pathway, Angew. Chem. Int. Ed. 61 (2022) e202205429.
[62] T. Liu, W. Liu, M. Zhang, W. Yu, F. Gao, C. Li, S.B. Wang, J. Feng, X.Z. Zhang, Ferrous-supply-regeneration nanoengineering for cancer-cell-specific ferroptosis in combination with imaging-guided photodynamic therapy, ACS Nano 12 (2018) 12181–12192.
[63] H. Wang, X. Li, B.W. Tse, H. Yang, C.A. Thorling, Y. Liu, M. Touraud, J.B. Chouane, X. Liu, M.S. Roberts, X. Liang, Indocyanine green-incorporating nanoparticles for cancer theranostics, Theranostics 8 (2018) 1227.
[64] T.G. Nguyen Cao, J.H. Kang, J.Y. You, H.C. Kang, W.J. Rhee, Y.T. Ko, M.S. Shim, Safe and targeted sonodynamic cancer therapy using biocompatible exosome-based nanosonosensitizers, ACS Appl. Mater. Interfaces 13 (2021) 25575–25588.
[65] S. Dong, Y. Dong, Z. Zhao, J. Liu, S. Liu, L. Feng, F. He, S. Gai, Y. Xie, P. Yang, "Electron transport chain interference" strategy of amplified mild-photothermal therapy and defect-engineered multi-enzymatic activities for synergistic tumor-personalized suppression, J. Am. Chem. Soc. 145 (2023) 9488–9507.
[66] G. Gao, X. Sun, G. Liang, Nanoagent-promoted mild-temperature photothermal therapy for cancer treatment, Adv. Funct. Mater. 31 (2021) 2100738.
[67] X.X. Yang, X. Xu, M.F. Wang, H.Z. Xu, X.C. Peng, N. Han, T.T. Yu, L.G. Li, Q.R. Li, X. Chen, Y. Wen, T.F. Li, A nanoreactor boosts chemodynamic therapy and ferroptosis for synergistic cancer therapy using molecular amplifier dihydroartemisinin, J. Nanobiotechnology 20 (2022) 230.
[68] K. Sun, J. Yu, J. Hu, W. Yang, X. Chu, L. Chen, X. Deng, B. Sun, Z. Wang, Photothermal enhanced polyphenol-based nanofibers ameliorate catalytic efficiency of ferroptosis for synergistic tumor therapy, Chem. Eng. J. 470 (2023) 144360.